RESPIRATORY-GATED LIVER STEREOTACTIC RADIOTHERAPY IN FLATTENING FILTER FREE PHOTON MODE

by

Tania Karan

A THESIS SUBMITTED IN PARTIAL FULFILLMENT OF
THE REQUIREMENTS FOR THE DEGREE OF

MASTER OF SCIENCE

in

The Faculty of Graduate Studies

(Physics)

THE UNIVERSITY OF BRITISH COLUMBIA
(Vancouver)

August 2013

Abstract

Respiratory motion makes radiotherapy of abdominal targets, such as the liver difficult. Respiratory gating is used to treat tumours in select portions of the respiratory cycle where their location is well known, increasing target coverage precision and reducing normal tissue damage. The tradeoff is an increase in treatment time, which can be partially overcome by using a higher dose rate, provided by flattening filter free (FFF) photon mode.

To validate that increasing dose rate through removal of the flattening filter does not decrease cell kill, radiobiological experiments were carried out with three cell lines. Both the clonogenic survival assay and γH2AX double strand break assay indicated that FFF mode does not negatively affect cell kill.

To form dosimetric and radiobiological bases for gated radiotherapy in FFF mode, a phantom was used to simulate respiratory traces of 10 patients previously treated for hepatic disease. Following 4DCT imaging, four plans were created and delivered for each respiratory trace; one nongated and three with the following gating windows: 80-20%, 40-60% and 30-70%. Treatments were delivered in 10MV FFF mode at 2400 MU/min, with optically stimulated luminescence dosimeters (OSLD) used for dosimetric measurements. OSLD doses were compared to those calculated by *Eclipse* Treatment Planning System. The plans were delivered to vials of cells to confirm whether dose to a moving target is compromised, changing cell survival. Dosimetry and survival was compared between the gated groups and also against the baseline – nongated treatment of a static phantom.

Discrepancies of up to 7% were observed between the planned and measured doses. Most gated plans showed Eclipse overestimating the physical dose to the OSLDs, however the reverse was true for nongated plans. The best correlation between Eclipse and OSLD dose was seen in nongated plans and plans with a short duty cycle during expiration. Significant differences in cell survival and metabolic activity were seen between the gated groups and could not be attributed to dosimetric differences. No trend was established for the gated plan that results in the highest cell kill. Dosimetrically this work concludes that gating in FFF mode results in acceptable variations in target coverage.

Preface

Parts of this work, largely from chapter 2, were published in the following article prior to submission of the thesis:

Karan T, Moiseenko V, Gill B, Horwood R, Kyle A, Minchinton AI. Radiobiological effects of altering dose rate in filter-free photon beams. Phys Med Biol. 2013;58(4):1075-82.

The research goal was proposed by V Moiseenko and AI Minchinton, evolving with student contribution. B Gill, R Horwood and A Kyle contributed to experimental design and procedures. Research, data collection and analysis as well as manuscript preparation were entirely completed by the student. Manuscript review and final approval was done by V Moiseenko and AI Minchinton.

A portion of this work, derived mostly from chapters 3 and 4 has been submitted for publication with approval pending. Research was proposed and guided by V Moiseenko, with student input elaborating experimental design. Research, experiments and manuscript preparation were entirely carried out by the student. All co-authors reviewed the manuscript, contributing ideas for improvement. Final manuscript approval was done by V Moiseenko.

Table of Contents

List of Tables

List of Figures

Abbreviations

6X – 6 MV photon mode

10X – 10 MV photon mode

10FFF – 10 MV flattening filter-free photon mode

AAA – Anisotropic Analytical Algorithm

AAPM – American Association of Physicists in Medicine

DPP – dose per pulse

CI – conformity index

DSB – double strand break

DVH – dose-volume histogram

FFF – flattening filter free

GI – gradient index

GTV – gross tumour volume

HI – homogeneity index

HVL – half value layer

IGRT – image guided radiation therapy

IMRT – intensity modulated radiation therapy

inf – inferior (anatomically, towards one's feet)

linac – linear accelerator

MLC – multi-leaf collimator

NSCLC – non-small cell lung carcinoma

NTCP – normal tissue complication probability

OAR – organ(s) at risk

OSLD – optically stimulated luminescence dosimeter

PRF – pulse repetition frequency

PTV – planning target volume

QUANTEC – quantitative analysis of normal tissue effects in the clinic

RILD – radiation induced liver disease

RTOG – radiation therapy oncology group

SAD – source-axis distance

SBRT – stereotactic body radiation therapy

SSD – source-skin/sample distance

sup – superior (anatomically, towards one's head)

TG – task group

VMAT – volumetric modulated arc therapy

Acknowledgements

This thesis is a product of people who trusted me enough to let me run a linear accelerator. Accordingly, I would like to extend a sincere thank you to the following:

All of the Medical Physics staff at BCCA for their guidance – particularly Richard Lee for teaching me all there is to know about gating. The physics assistants – Vince S, Vince L and Ron – for guiding me in operating the wonderful, if temperamental TrueBeam linac. To the members of the Minchinton Lab – Alastair, Jenn, Kirstin, Jordan and MJ, who provided a wealth of knowledge outside my realm and created a great interdisciplinary environment. To my family and friends, who were the balance I needed to make the graduate experience a pleasant one.

Eternal gratitude goes to Stefan Reinsberg for the persistent support of my academic career and Brad Gill, who by chance became a supervisor and an important mentor. Lastly, my successes are fully owed to my research co-supervisor Andrew Minchinton and supervisor, Vitali Moiseenko. Thank you for your encouragement, tireless support and keeping a good sense of humor throughout the process.

1 Introduction

1.1 Liver SBRT

Stereotactic radiotherapy arose as a single high dose treatment for brain metastases using a Cobalt-60 gamma knife at the Karolinska Hospital in Stockholm, 1975. Stereotactic extracranial, or body, radiotherapy (SBRT) formed as an extension of its cranial counterpart, with first patients receiving treatments in the span of 1991-1995 likewise at the Karolinska Hospital (1). Treating with SBRT is most often associated with lung and liver tumours. This modality has, however, shown promise in treating pancreas, prostate and spine lesions and has been suggested as an option for primary renal cell carcinoma treatment (2).

The most established SBRT treatment is for lung tumours. Conventional fractionation for treatment of lung cancer consisted of 2 Gy fractions given five times weekly for a total of 60-70 Gy (3). Standard treatments resulted in poor local control, consequently a need for dose escalation as well as altered fractionation schedules arose (4). Accordingly, SBRT arose in the form of 3 fractions of 8 Gy (5) and then three fractions of 20 Gy (6) for treating medically inoperable lung cancer. In recent years there has been a trend in treating operable lung tumours with SBRT because the results are just as good or better than with surgical resection (7, 8). SBRT has thus emerged as the standard of care for treatment of stage I non-small cell lung carcinoma (9-11). Radiation therapy oncology group (RTOG) 0236 summarizes the eligibility requirements for SBRT treatment of non-operable non-small cell lung cancer (NSCLC). The cancer must be at its early stages, with the primary tumour limited to the chest wall and ≤ 5 cm in size, with any suspicious lymph nodes biopsied and negative for the disease (12). Patients with a tumour in the volume defined as 2 cm surrounding the bronchial tree are not eligible, as are patients with previous lung radiotherapy. Similarly, RTOG 0618 for treatment of operable stage I/II NSCLC has the same requirements, and further for the primary tumour to be technically resectable with a high probability that the resection margins will not encapsulate the whole tumour. SBRT treatment covers a larger volume than resection, ensuring that more of the tumour margins will get the necessary lethal dose.

SBRT itself does not require different equipment than the readily available radiation oncology tools. Units with image guidance, multileaf collimators and support systems with greater degrees of freedom contribute to the ease of treatment. SBRT is characterized by immobilization devices such as body frames constructed specifically to minimize movement of the target and surrounding normal tissue during treatment. SBRT differs from conventional radiotherapy in that all processes including imaging, planning and treatment require an enhanced level of precision seeing as the doses delivered can be very harmful if the resultant distribution is inaccurate (13). For such high doses to be delivered while maintaining normal tissue dose limits, sophisticated treatments must be employed often involving multiple non-coplanar fields or arcs.

Treatment with SBRT rather than conventionally fractionated radiotherapy leads to an increase in biologically effective dose (13), likely due to a combination of various radiobiological effects addressed in the following section. The shortened course of treatment offered by SBRT provides less of an opportunity for a tumour to repopulate between fractions. And while conventionally the objective of radiotherapy is seen as killing tumour cells, at doses above 10 Gy cell lethality is no longer determined solely by damage produced within cells. The environment, including the extracellular matrix as well as the processes such as nutrient supply have been found to play larger roles in radiation injury than previously thought. An increasingly popular idea revolves around damage to tumour vasculature as the primary instigator to tumour eradication (14). Animal studies show that single high dose treatments trigger endothelial cell apoptosis pathways that are not present in fractionated regimes (15). Various immune responses likewise vary with accumulated dose, though their quantification proves more difficult (16, 17).

Liver tumours occur most commonly in the larger, more vascularized right hepatic lobe and are more often a result of metastases rather than being primary liver cancers (18). Primary cancers are most often hepatocellular carcinomas (HCC) and less often cholangiocarcinomas (<400 cases/yr in Canada while metastases occur from many sites most often originating as colorectal, pancreatic and gastric cancers. From 1969-1997 age-standardized HCC incidence rates in Canada increased 3.4% / year in males and 1.2% in females (19). More than 50% of primary colorectal cancer cases result in liver metastases which occur via portal vein drainage (20). 2000 cases of primary liver cancers were reported in Canada in 2012, however 23,300 cases of colorectal cancer occurred accounting for 12% of all cancer deaths (Canadian Cancer Stats

2012) – usually through metastasizing. The significance of liver lesions impairing the organ's function lie in the many life-sustaining roles the liver is responsible for – most notably glucose and fat metabolism, protein and hormone synthesis, urea production and detoxification (21).

The primary method of treatment is as for most cancers, surgical resection when possible. However only 20% of HCC masses (22) and 25% of liver metastases (23) are suitable for resection. Cases that do not meet the resection criteria occur when the non-cancerous liver tissue is deemed unhealthy due to other causes such as cirrhosis, indicating resection would leave too little healthy tissue for liver regeneration and function. Other instances that do not allow surgical intervention involve cancers that have already spread through the liver and occur close to hepatic veins, arteries and bile ducts making surgery not possible without posing a great risk to vital hepatic structures.

Non-surgical hepatic malignancy treatments include any of percutaneous ethanol injections, chemoembolization, cryoablation or radiofrequency ablation (24). Such treatments are invasive, often not suitable for large lesions and suffer from non-specificity to tumours at times causing considerable pain in the patient. Most importantly, the patient survival following such treatments is nowhere near the gold standard – resection. A new avenue in terms of stereotactic radiotherapy provides an alternative to surgical resection. The tolerance of the liver has lead to large prescribed doses ranging from 45 Gy in 3 fractions over 5-8 days (25) to 75 Gy in 3 consecutive daily fractions (26). Further, maximum doses allowed in the PTV range up to 140% (23) of the prescribed dose, not an unusual strategy in SBRT. Stereotactic radiotherapy aims to deliver very large radiation doses to targets while maintaining minimal dose to surrounding normal tissue thus requiring ultra-precise patient imaging and positioning (27).

In addition to normal hepatic tissue, the surrounding organs at risk are most often the kidneys, duodenum and stomach (28, 29). Since normal tissue injury is the limiting factor to radiotherapy, SBRT poses an even greater risk due to the sensitivity of normal tissue to fraction size. AAPM's TG101 report (13) discusses recommendations for the maximum critical volume of normal tissues to receive maximum point doses in case of serial organs, or threshold doses for parallel organs. The doses are recommended for three common fractionation schemes. <10 cc of the stomach and <5 cc of the duodenum ought to receive <12.4 Gy in one fraction, <22.2 Gy in three fractions or <32 Gy in Gy in five fractions. For the liver the recommendation is that >700 cc receives maximum threshold doses of 9.1, 19.2 and 21 Gy in 1, 3 and 5

fractions respectively. The significance of the liver in bodily functions warrants a further look at its radiation injury.

1.1.1 Radiation induced liver disease

The dose-limiting factor in liver treatment is the risk of radiation-induced liver disease (RILD). To address the anatomical and physiological considerations in RILD, it is best to provide an overview of two investigations published by groups at University of Michigan followed by guidelines established by QUANTEC. Classic RILD generally appears 4-8 weeks after the end of treatment, presenting as fatigue, weight gain, hepatomegaly and discomfort in the right upper chest area (30). What is known as 'non-classic' RILD refers to patients with other chronic liver disease like hepatitis that do not have the above-mentioned symptoms but present with abnormal liver function. Diagnosing RILD through CT imaging is difficult since a lower density of liver tissue is seen for areas treated with radiation regardless of the presence of RILD status. Imaging in addition to physical exams can however reveal presence of ascites and hepatomegaly. Furthermore, laboratory tests measuring elevation of alkaline phosphatase and aspartate transaminase enzymes are effective in diagnosing RILD. Patients with classic RILD generally show normal function and enzyme levels, while those with non-classic RILD will have markedly high enzyme levels following radiation treatment (31).

A prognostic factor in RILD is the concurrent administration of chemotherapy. The primary concern for RILD in radiation therapy is dose-volume effects. Dawson et al. (32) used the Lyman normal tissue complication probability model to re-evaluate plans of 203 previously treated patients who were screened for RILD following radiation treatment of their intrahepatic liver cancer. The median dose delivered was 52.5 Gy, in eleven 1.5-1.65 Gy fractions per week given twice daily. It was found that livers of patients with primary malignancies were more sensitive to radiation than those with metastases, although a confounding effect was that primary lesions were sometimes accompanied by pre-treatment cirrhosis or hepatitis. A worsening of such preexisting conditions is recognized as one of several types of liver injury.

The QUANTEC organ-specific paper focusing on the liver provides a review of dose-volume data resulting tentative guidelines aimed at minimizing risk of RILD (33). QUANTEC extends the timeline for typical RILD occurrence to 2-3 months following treatment completion, focusing on much the same clinical endpoints as the previous papers. Challenges defining the volume of the healthy liver tissue are addressed, particularly due to motion. Two aspects in radiotherapy are recognized by QUANTEC as having clinical significance; the mean dose to the whole liver, and the volume receiving over 30 Gy. Acknowledging that long term injury of the liver has not been established, QUANTEC provides the following broad dose-volume guidelines for a <5% risk of RILD in SBRT of the liver (reprinted with permission of Int. J. Radiation Oncology Biol. Phys. (33) via RightsLink) :

Nonuniform liver recommendations (SBRT, three to six fractions)

Mean normal liver dose (liver minus gross tumor volume)

< 13 Gy for primary liver cancer, in three fractions

< 18 Gy for primary liver cancer, in six fractions

< 15 Gy for liver metastases, in three fractions

< 20 Gy for liver metastases, in six fractions

< 6 Gy for primary liver cancer, Child-Pugh B, in 4–6 Gy per fraction (for classic or nonclassic RILD)

Critical volume model-based

≥ 700 mL of normal liver receives ≤ 15 Gy in three to five fractions

1.1.2 The clinical experience

Most liver SBRT studies use various outcomes as endpoints including but not limited to local disease progression/control, progression free survival inclusive of intrahepatic and sometimes extrahepatic metastases and overall survival. Schefter and Kavangh review radiation therapy for liver metastases, SBRT being a key method of interest. Most studies showed above average, if not excellent

outcomes in terms of improved local control with no dose-limiting toxicities observed (34). For example, the dose escalation study of Rule *et al.* showed 100% actuarial control rates for patients treated with 60 Gy in 5 fractions (35). Studies that did not show significant improvement often suffered from issues confounding effects.

Indeed the at times insignificant improvement in phase I/II patient liver SBRT trials can largely be attributed to the nature of patient selection. Many patients did not have primary tumours or metastases solely isolated to the liver, thus treatment of the liver cannot be used as a measure for overall cancer eradication. Most exclusion criteria do not take into account the aggression of the primary tumour, which may or may not be concurrently treated, though spread of disease to lymph nodes and distant sites generally made patients ineligible for studies. Certain patient inclusion criteria required lesions to be smaller than 5-6 cm in diameter and 3-5 in number (18, 36) while others had no limit to maximum tumour size or number (23). The inclusion criteria are much looser than those of other treatments, thus radiotherapy can be seen as a last measure of treatment in many instances. These circumstances lead to somewhat poor statistics in cases where patients died as a result of extrahepatic tumour sites or further metastases before the follow-up deadlines. The local control of the hepatic SBRT sites is difficult to determine due to outside factors (36). Certain studies show that local recurrence is more common in tumours that are close to large vessels and have a diameter >4cm, in other words, candidate tumours for SBRT (22). Most of the previously mentioned studies ensure patient comfort and safety by delivering a dose or escalating to a dose where dose-limiting toxicity does not occur (18, 22, 23, 36, 37). In this way, it is difficult to know how large of a dose can be effectively given and the impact on liver lesions.

A further issue in liver SBRT outcomes arises from local control reporting due the difficulty of distinguishing radiation effects from recurrent tumours. Liver tissue is isodense to tumours, thus contrast agents are often required for precise tumour localization and delineation. Further complicating the imaging process is the phenomenon that irradiated areas of the liver become hypodense relative to the spared portions (38). Treated tumours will largely still appear as areas of much lower density than the irradiated areas, however in select cases it may lead to the radiation reaction being deemed a recurrent tumour. Such issues may imply there is a need for standardization of imaging protocols in studies following SBRT liver patients.

Dose conformity has allowed for escalation with improved local control and no increase in RILD occurrence. Although SBRT data has accumulated for a decade, most experience is with lung treatments. The most efficient approaches for treating the liver are still under development and clinical testing, and in particular the biggest hurdle is the respiratory-induced movement during imaging and treatment.

1.2 The radiobiological effects of SBRT

The report of AAPM's task group 101 (13) discusses the definition and guidelines for stereotactic body radiation therapy. Their comprehensive summary states that the majority of cases treated by SBRT are for lung, liver and spinal tumours which have discernable margins and are generally less than 5 cm in diameter. The benefit of delivering fewer but larger radiation fractions is said to be increased biological effectiveness.

Delivering a large dose in a single or few fractions holds implications for all aspects of the radiobiological response to radiation. The effects must be distinguished for the target – namely a tumour – and early and late responding tissues. It is necessary first to define what stereotactic treatments entail – they can be considered as an extreme form of hypofractionation. The course of an entire treatment is generally shortened since doses are delivered in 3-5 fractions with approximately 2 fractions per week. In accordance with the biologically effective dose model, treatments also generally require an alpha/beta ratio and fraction size-dependent increase in the isoeffective dose.

The benefit provided by hypofractionation is somewhat dependent on the tumour growth rate. Throughout literature, doubling times for liver malignancies are on the order of 6 weeks (metastases) to 11 weeks (recurrence). Johnson *et al.* (39) found that hepatocellular carcinoma has a doubling time of 41 days, deeming it a rapidly proliferating tumour. Though values differ through literature, there is somewhat of a consensus that liver tumours (primary, metastatic and recurrent) all have a relatively short doubling time. The biggest benefactors of hypofractionation, however, tend to be slow growing tumours such as those of the prostate, which generally have a smaller alpha/beta ratio and are thus more sensitive to doses per fraction. In such cases fractionation acts to lower the viable fraction of tumour cells able to repopulate a tumour, and the increase in size is insignificant at time of the next fraction. Hypofractionation on its own can therefore be seen as providing little benefit to the more rapidly dividing liver tumours.

The temporal effect of great significance in duration of radiotherapy treatment is accelerated repopulation. Often tumours undergo a rapid onset of repopulation following radiation therapy, once functional injury has been registered by the tissue (40). The idea behind shortening overall treatment duration to offset accelerated repopulation is relatively old – prior to advances in conformal therapy this was done through hyperfractionation and multiple doses per day (41). Historically, the rapid spike in repopulation for head and neck cancers, for example, is known to occur ~28 days following the beginning of radiation treatment (42), thus efforts are made to keep total treatment time shorter than a month. The continuous, hyperfractionated, accelerated radiotherapy (CHART) trial (43) studied the effect of delivering treatment 3x daily for 12 days as opposed to standard treatment of 2 Gy 5 times a week for treatment of non-small cell lung carcinoma. A histology-dependent improvement was seen in overall survival, local tumour control, as well as disease and metastases free survival in the CHART arm of the study. More recently hypofractionation and larger doses such as in SBRT have proved beneficial. If the course of treatment exceeds the time of repopulation kickoff, it has been found that fewer larger fractions are advantageous (44). A CHART trial for head and neck cancer compared conventional fractionation, 2 Gy 5 times a week for a total of 66 Gy to an accelerated treatment consisting of 1.5 Gy three times daily for 12 consecutive days for a total of 54 Gy. Their results implied that tumour control, nodal control, and disease and metastases-free survival showed no significant difference in the two treatment methods (45).

Tumour reoxygenation is known to occur following a radiation fraction due to the selective killing of well oxygenated cells, and reducing tumour size which in turn can increase the proximity of hypoxic cells to oxygen-rich blood vessels. As such, fractionation is beneficial in sensitizing hypoxic tumour cells by increasing their oxygen supply in one fraction, and eradicating them the next (46). Delivering treatment in fewer fractions, such as in SBRT, reduces this extra oxygen-enriching step reducing the sensitization of cells. Initially it was thought that the ablative nature of SBRT induced such a large amount of damage that oxygen was no longer a factor. More recently, the idea that more mild hypofractionation, such as eight as opposed to three fractions which are common in SBRT, may be more beneficial in tumour control. Ruggieri *et al.* (47) have provided a mechanistic model that found acutely hypoxic cells responsible for repopulating an irradiated tumour. They found that tumour control probability, through destruction of the acutely hypoxic cells benefits from increasing the number of SBRT fractions from three to eight.

Once again it is necessary to emphasize that the dose prescription in radiation therapy is dictated by normal tissue complication probability. Since healthy tissues generally have an alpha/beta ratio that is lower than tumours, the sparing effect of fractionation is lost. Normal tissues are more resistant to low doses than tumours, which have a high alpha/beta ratio, thus delivering treatment in multiple fractions enables proportionally more tumour control for the same amount of normal tissue damage. The converse is true for hypofractionation – tumours are more sensitive to the total dose than fraction size, but a greater normal tissue complication probability arises when larger doses are delivered in one fraction. Certain tumours, however, have alpha/beta ratios very similar to those of normal tissue, and may benefit from hypofractionation. In parallel organs such as the liver the volume effect dictates that a large region may get sacrificed with the remainder of the organ compensating for its function. As such, very large doses may be delivered to the liver, as long as the critical volume is left undamaged so that function is not impaired.

The increase in normal tissue damage has in recent years been well addressed through technological advances enabling great dose conformity and organ sparing, such that this increase in predicted risk of normal tissue complications is somewhat offset (48-50). An issue that has not been accounted for is the fact that such high doses in one treatment session cause tissue response changes. High doses have shown to change injury response of tissue from fibrotic to atrophic, which is clearly demonstrated by occurrence of rib fractures in stereotactic treatment of lung tumours (51-53). With this variety of competing effects in SBRT, it remains to be seen whether this treatment modality will be beneficial to treatment of the liver. Positive outcomes in lung SBRT are well established and encourage further trials in SBRT of the liver as well as other sites.

1.3 Gating

AAPM's task group 76 discusses the various methods of accounting for respiratory motion during treatment among which are: motion-encompassing, respiratory gating, breath-hold, forced shallow breathing and respiration-synchronized techniques (54). The collective discussion of motion tracking indicates that authors have used methods such as embedding fiducials into the tumour and tracking a host or surrogate organ among others. The imaging modalities to ascertain location of the tumour are as numerous as the methodologies; ultrasound, fluoroscopy, cine computed tomography and magnetic

resonance imaging are all capable of resolving tumour location in time. Displacement and phase gating using an external, infrared marker to track motion of the chest during CT imaging and treatment are discussed as methods currently under study for efficacy in treating various moving tumours. Stress is placed on treating patients on a case-by-case basis because respiration patterns and the ability to breathe in a trained manner as is required for breath-hold and gating methods vary by individual.

The limiting factor in radiation therapy is the maximum allowed dose for normal tissue surrounding radiation targets. The unavoidable movement of abdominal and thoracic targets makes it difficult to deliver sufficiently large doses to targets whilst remaining within normal tissue limits. Gating is introduced as a method that enables the delivery of large doses to sites while complying with normal tissue guidelines by selectively turning a photon beam on when the target is in a certain location. The geographic location of a target closely corresponds to the phase of a respiratory cycle in which it occurs, thus by quantifying and characterizing a patient's respiration, certain phases can be chosen for treatment. Common sites for this type of treatment are mostly lung, more recently liver, pancreas and even breast carcinomas. The treatments require 4D image sets usually acquired via CT coupled to a tracker of respiratory phase. Planning must also be done in 4D, selecting phases of the respiratory cycle during which the beam is delivered.

The duty cycle is a ratio of gate duration to the complete respiratory period and its precise assignment is of utmost importance to gating. Since most research shows that a greater amount of time is spent in the expiration part of a respiratory cycle, generally plans are created such that beam-on will occur for some gating window during expiration. Likewise advantageous in treatment, there is an argument that organ location is more reproducible in expiration than inspiration. In the treatment of non-small cell lung carcinoma, an opposing argument arises since inspiration expands the lungs, distancing normal tissue away from the radiation beam path hence resulting in less normal tissue damage, a dosimetric advantage (55). Still, no such advantage is assumed for the liver since it's motion is simply a product of its vicinity to the lungs and diaphragm. The gating window is a compromise between optimizing the duty cycle allowing for longer beam on time, and normal tissue complications remaining minimal.

The gross tumour volume (GTV) is defined as the discernable extent of a tumour, which may be visualized through imaging or alternatively palpated by a physician. Furthermore, most oncologists will

define a clinical tumour volume, which is an extension of the GTV to account for possible microscopic or non-visualized disease. To account for possible motion of the tumour, an internal target volume (ITV) can be defined and extended to include a tumour in full extent of its motion. In 4D imaging and treatment, an ITV encompasses a tumour in all parts of the respiratory cycle. A further structure, the planning target volume (PTV) is drawn with an extension around the ITV, to account for setup uncertainties such as the discrepancy between laser alignment in CT and treatment unit, and uncertainties in aligning a patient on the treatment couch. The extent of the contoured structures will depend on the amount of motion present at specific treatment sites. As shown in Figure 1.1, motion of the target greatly increases the volume of irradiated surrounding tissue, an obstacle overcome by gating. The downfall, of course is the need to prolong overall treatment time since beam-on occurs only for a portion of a respiratory cycle .To overcome this problem, a greater dose per fraction may need to be delivered to counteract the decreasing efficacy at prolonged treatment times.

Figure 1.1 PTV and ITV contours in gated and nongated plans

Reprinted with permission from the Int. J. Radiation Oncology Biol. Phys. (56) via RightsLink.

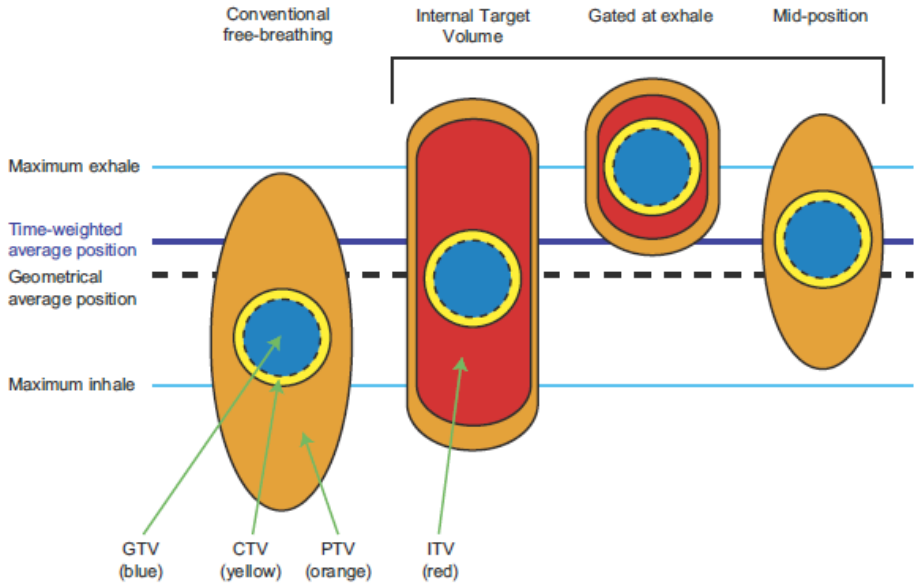

The risk of RILD makes further dose escalation in SBRT of liver lesions a costly attempt. The

respiratory-induced liver motion can be quite significant, as summarized in Table 1.1. The contraction of the diaphragm moves the liver in the supine direction while the anterior organ side rotates slightly rightward (57). The span of the liver has been estimated to be anywhere from 6-12 cm along the midclavicular line, thus the relative motion is significant compared to organ size. Respiratory gating enables sparing a larger part of the liver while delivering large doses.

Table 1.1 Summary of liver motion from various studies

Extent of liver motion for normal and deep breathing. Reprinted with permission from the Int. J. Radiation Oncology Biol. Phys. (58) via RightsLink.

			Normal breathing PTT (mm)		Deep breathing PTT (mm)	
Study: first author (ref)	No. of patients	Patient position	Avg ± SD	Range	Avg ± SD	Range
Weiss (40)	25	Standing	8 ± 2			
	25	Supine	11 ± 3			
Harauz (41)	51	Standing	12			
	51	Supine	14			
Suramo (42)	50	Supine	25	10–40	55	30–80
Davies (43)	9	Supine	10 ± 8	5–17	37 ± 8	25–57
Balter (44)	9	Supine	17			
Shimizu (45)	1	Supine	21			

PTT = peak-to-trough.

1.4 Flattening filter free photon mode

Flattening filters have constituted a standard part of a linear accelerator's design since the 3D conformal era of radiotherapy, when modulation was not employed. Their presence stems from the need to create a level photon dose profile from an otherwise forward-peaked beam of photons. This was a necessity in treatment planning that relies on even photon intensity, an issue that has since been overcome through the evolution of treatment planning algorithms. Intensity modulated radiation therapy (IMRT) relies on the modulation of a photon beam, such that starting with a non-flat beam profile is easily accounted for. Removing the flattening filter increases MU rate from 600 to 1200 MU/min for 6MV photons, and from 1200 to 2400 MU/min for 10 MV photons.

The feasibility and safety of using FFF beams in SBRT has been demonstrated by Scorsetti *et al.* (59) who noted the FFF radiotherapy patient cohort did not exhibit adverse acute effects following treatment of a much higher dose rate. A clinical trial for patients with liver tumours (primary and

metastatic) treated with FFF SBRT showed that a higher dose can be achieved within the PTV as well as the organs at risk, however the doses were still within limits (26). Reggiori *et al.* carried out treatment optimizations for virtual hepatic lesions of various sizes contoured on a patient's CT and compared the treatment plans for filtered vs. FFF 10 MV photon beams (60). They found medium-sized tumours benefited the most in terms of dose conformity when treated with FFF rather than filtered plans. In terms of dose homogeneity the biggest advantage was posed to small tumours when using FFF mode. Overall the performance of FFF beams as measured through various methods is the same as their filtered counterparts, if not improved. The limitation of an uneven dose profile remains as a hurdle to treatment with a large target, which requires beam 'painting' in FFF mode.

In conjunction with gating, FFF mode of photon delivery reduces intrafraction motion (59) by decreasing the time over which a certain dose is delivered. This allows for defining a target in a certain part of respiration where its volume is smaller and location well known. As such FFF mode is an excellent candidate for gated radiation therapy, allowing for a shorter duty cycle decreasing overall treatment time.

1.5 Outline of the study

Currently, there is a paucity of studies exploring the radiobiological effects of gating. The following thesis combines above-discussed aspects into a study of dosimetric and radiobiological implications of combining the FFF modality with gated radiotherapy. To validate that use of FFF beams has no negative implications on cell survival such as a reduction in cell kill, various radiobiological experiments comparing clonogenic survival and induction of double strand breaks were carried out in filtered and FFF mode. As a precursor to gating experiments, experiments were also done to measure the effect of dose protraction on cell viability.

Due to its high instantaneous dose rate, the utility of FFF photon beams in gated treatments is recognized but remains to be dosimetrically verified. In decreasing treatment time, narrower gating windows may be selected at no risk to underdosing targets. The following study creates a dosimetric basis for gated treatments in FFF mode through use of a phantom capable of simulating patient respiratory motion. Altering treatment time requires a radiobiological consideration as temporal effects are of great

importance in cell damage processes. Survival and viability cell assays are presented in the following work as a means to developing a radiobiological basis for gating in FFF mode.

It is important to note that although the author acknowledges that normal tissue injury is the main factor of importance in radiation treatment, this study is a validation of dose to the target and in no way describes dose to surrounding normal tissue.

2 Flattening Filter Free Photon Beam Mode

2.1 Overview

2.1.1 Dosimetric Advantages

Flattening filters made of high-z materials such as lead or tungsten are used to create uniform beam intensity in linear accelerators, however they lead to other effects on beam quality. Filtered accelerators suffer from beam hardening due to selective attenuation and beam softening due to Compton scattering and filter geometry (61). Findings indicate that variations in half-value layer with angle (62) as well as differences in depth of maximum dose deposition with field size (63) are both more pronounced in filtered than filter-free photon beams. The steeper dose fall-off in unflattened beams (63) holds implications in reducing dose to normal tissue beyond the target. A further dosimetric advantage for FFF beams is seen in the reduced variation of the head scatter factor (64), which largely induced by the presence of a flattening filter in he head of a linac (65).

The biggest issue of FFF beams for radiotherapy is the non-uniform dose-distribution created by an unfiltered beam. This can be overcome, since for field sizes smaller than 5x5 cm, the beam profile varies only slightly (65), and large field sizes are generally not used in stereotactic radiotherapy. IMRT relies on altering beam intensity, and incorporating beam shape into dose planning is not overly difficult. A filtered beam will have a different overall energy due to the various effects leading to hardening and softening which aren't present in a FFF beam, however beam energy can be altered by adjusting linac parameters (64). Removing the flattening filter of a linear accelerator may therefore cause fewer errors in dose-delivery and scatter affecting normal tissue, as well as ease the transition from smaller to bigger field sizes.

The most apparent advantage of a FFF method of beam delivery is an increase in the dose-rate. Varian TrueBeam linear accelerator has the capability of reaching a dose-rate of 1200 MU/min with a 6 MV photon beam, or 2400 MU/min with a 10 MV beam in FFF mode, with an approximate uniform 2 cm beam intensity surrounding the central axis. This capability enables shorter treatment times due to a doubling in dose rate thus increasing patient throughput. In treatments involving setups such as chest compression, which are inconvenient for the patient, a decrease in treatment time may mean a significant

improvement in patient comfort. An increase in dose rate likewise holds positive implications in all methods that account for tumour motion. In breath hold treatments, the patients can either do fewer or shorter 'holds' while still getting the same dose. In gating, either the total treatment time or duty cycle can be reduced.

The reduced treatment time becomes particularly important in fixed-field IMRT and VMAT treatment plans. Due to the modulation of the photon beam, a sharp increase in the number of monitor units is required to deliver the same dose as in non-modulated plans. Complex IMRT fractions can take15-30 minutes to deliver, although the RapidArc method is an improvement due to the continuous gantry motion and dynamic multi-leaf collimation leading to treatment times of 1-3 minutes for a 2 Gy fraction (66-70). Stereotactic doses are, however, on the 10-20 Gy order such that a fraction can take 30 minutes to deliver even using RapidArc. In this regard, a reduction of treatment time to half of the original due to availability of FFF mode proves a great benefit.

2.1.2 Possible Radiobiological Effects

Any effect due to dose-rate occurring at prolonged treatment times is generally attributed to the repair of sublethal lesions, therefore most research thus far has centred on comparing dose rates of 1 Gy over hours to 1 Gray over minutes (71-75). Many studies to date have shown that tissue response does not follow the initially hypothesized mono-exponential repair model in the hours following radiation (76). The number of unrepaired DNA breaks is inversely proportional to the time following irradiation, however data also suggests that the rate of repair depends on the amount of damage, thus repair occurs more rapidly when there is more damage present. A bi-exponential repair model has been suggested as a good alternative, proving to be a better fit for repair plotted in time. The improved fit was observed in rat spinal cord (77) models as well as porcine and human skin (76, 78). In addition to establishing that repair consists of a fast and slow component, the bi-exponential fits often showed that the fast component is responsible for most of the repair, Rongen et al. (79) suggesting a value of 80% for the proportion of damage repaired by fast repair. Alpha/beta ratios serve as an inverse measure of the capacity for repair, thus implying that early-reacting normal tissue has similar repair rates to tumours, confirmed by similar, relatively short repair

half-times (80). Considering that even the fastest repair rate for both tumours and normal tissue has a half time on the order of 20-30 minutes (81), dose-rate effects are unlikely in SBRT with or without the flattening filter, since treatment time is generally not comparable to repair half time.

The cell cycle effect has also been studied in relation to dose-rate. Implying cells' changing radiosensitivity in the different phases of the cell cycle, the effect favors lower dose rates in killing more cells (82). This occurs due to the fact that cells damaged by IR will not leave the G2 phase until this damage is repaired. Continual, low dose rate irradiation therefore leads to an increase in the radiosensitive, G2-bound population which is more prone to cell death by IR. The cell cycle effect is irrelevant at any dose rates used by TrueBeam, since treatment times will generally not exceed 30 minutes.

A further factor that may be of importance in the dose-rate effect on cell death is radiation-induced hypoxia. Ionizing radiation creates reactive oxygen species (ROS) that can damage cells through direct and indirect DNA interactions, such as cytokine release and activation (83). Injury of endothelial cells leads to vascular damage which in turn leads to inflammatory responses releasing more cytokines and the positive feedback loop continues. In this manner, vasculature feeding tumours is damaged, preventing oxygenanation. Furthermore, radiolytic processes deplete dissolved oxygen at a rate of approximately 1% / 3 Krad (84). The depletion rate would not alter treatment outcome unless a very large dose (as in stereotactic radiosurgery) is being delivered, and even so the hypoxic fraction would not acquire radioresistance during the same treatment time

Radiation creates damage in cells via two mechanisms. The first is direct, in that electrons that are emitted due to X-ray processes interact with the sugar-phosphate backbone of DNA inducing a double strand break. The second mechanism responsible for the vast majority of biological damage caused by X rays is the indirect effect in which radiation interacts with water molecules within cells creating free radicals that cause DNA damage. Mammalian cells are composed of 80% water (85), which reacts with photons to produce the shortlived radicals H• and OH•. The radicals are highly reactive due to unpaired electrons in their valence shell, and thereafter they will either recombine to reform stable products, like water (86), or go on to form other radicals and damage DNA through the process of ridding themselves of the outer electron. The likelihood of all the reactions is dependent on the temporal and spatial distribution of the ionizations creating radicals (87). Generally, linacs use a dose rate of 400-600 MU/min delivered in 2

μsec pulses at 300 Hz, with instantaneous dose rates reaching 10^6 MU/min (81). Linacs with a FFF mode capability, such as TrueBeam provide a greater instantaneous dose rate. We may assume the lifetime of the hydroxyl radical is $2.9x10^{-9}$ seconds, in which it moves approximately 25 Å (88). Increasing the dose-rate of irradiation increases the number radicals formed per unit time, thus the radical proximity may lead to the process of radical-radical recombination in turn reducing DNA damage. While this notion remains true in theory, it has been well established that linear accelerator dose rates, even in FFF mode are nowhere near high enough to see any decrease in damage effected by altered radical interactions.

2.2 Methods

2.2.1 Cells

H460 (human non-small lung carcinoma), V79 (Chinese hamster lung fibroblasts) and SiHa (human cervical carcinoma) cells were purchased from *American Type Tissue Culture*. All three cell lines were thawed and thereafter maintained in minimal essential media (*Sigma*) supplemented with 10% fetal bovine serum (*Gibco*), and kept in a 37°C, 5% O_2, 5% CO_2 incubator. On the day of the experiment, the cells were collected in media at a concentration of ~10^6 cells/ml, and 700 μL of the cell solution was placed into each of 22 custom clear glass vials (d=8 mm, l=24 mm). An aliquot of the cell solution was counted using a Beckmann Z1 Coulter Counter. After collection, cells were kept at 37°C until they were irradiated. The cells were irradiated within 1-2 hours of collection.

2.2.2 Dose Rate Effects in Acute and Split-dose Deliveries

Varian's TrueBeam STx (Varian Medical Systems, Palo Alto, CA) linear accelerator was used to carry out all irradiations. Vials of cells were placed on a jig submerged in a 37°C circulating water bath, with 5 cm of water both below and above the vials for scattering conditions. Cell samples were irradiated at a source-sample distance of 100 cm. In FFF mode a 10x10 cm field size provided an approximate 2x2 cm

uniform intensity surrounding the central axis at SAD=100 cm. The size of vials enabled two samples to be irradiated simultaneously whilst remaining in the uniform area. Prior to and after irradiation cells were kept at 37°C.

In the first experiment, 6X FFF mode was used and the MU rate was varied to either 400 and 1200 MU/min. Cells were irradiated with either 5 or 10 Gy (H460, V79) and the surviving fractions were compared. SiHa cells received doses of 2 or 5 Gy, because the surviving fraction at 10 Gy was deemed unreliable due to the cells' radiosensitivity. The second experiment involved irradiating cells with doses discussed, but maintaining a constant MU rate – 400 MU/min, while the beam was either filtered or not.

Finally, H460 and V79 cells were irradiated with 10 Gy in FFF mode using a split-dose regime over 15, 30 or 60 minutes. The 10 Gy was delivered in 11 identical fractions equally spaced in time (see scheme in Figure 2.1. This dose was selected to represent SBRT and mimic potential effect of gating.

Figure 2.1 Dose protraction scheme

Each evenly spaced fraction consists of an equal number of monitor units for a total of 10 Gy.

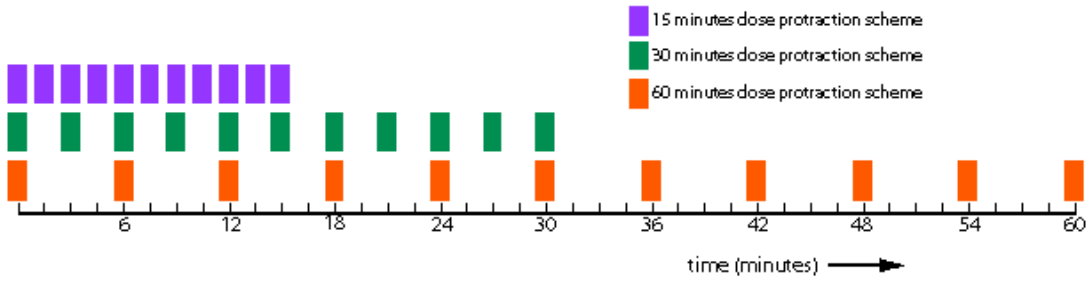

After irradiation, cell samples were diluted and counted, and $1/SF_{dose}$ cells were plated in a randomized manner into 10 cm tissue culture dishes (*Sarstedt* 100x200 mm) filled with 10 ml of media. The plates were incubated for 6 days (V79) or 11 days (H460, SiHa) to allow for colony formation. Thereafter media was removed from the plates and the colonies were fixed and stained using a 75% purified water, 25% abEtOH and 0.1% crystal violet solution. Only colonies containing 50 or more cells were counted, and the plating efficiency was determined by plating nonirradiated cells otherwise treated identically to those irradiated.

2.2.3 γH2AX DSB Assay

The reproducible nature and robust visual representation made the γH2AX assay a preferred secondary indicator to confirm and support the survival assay results. H460 cells subcultured as above were seeded onto 8-well glass slides (*Millicell*) at a concentration of 25,000 cells in 0.5 ml media per well two days prior to treatment. The cells were irradiated with 10 Gy at 400 MU/min in 6F or 6FFF mode at SAD=100 cm with 5 cm of solid water both above and below the cells. The cells were returned to the incubator, and fixed in 4% paraformaldehyde at one of two time points (1 hour or 24 hours) following the radiation treatment. Cells were stained with nuclear marker Dapi (*Sigma-Aldrich*) and for the presence of double strand breaks with mouse anti- γH2AX (*Millipore, clone JBW301*) and goat anti-mouse 546 (*Alexa Fluor*) antibodies. The fluorescence microscopy images were analyzed in *Image J* using custom software written by AH Kyle. Overall γH2AX fluorescence was quantified in place of counting foci since the images were taken at a single z-slice.

All experiments were performed with n=4 or more sample replicates, and repeated three or more times. All graphs show mean and error bars indicating standard deviation. A 2-tailed unpaired t-test with Welch's correction was applied to all pairs of treatment comparisons.

2.3 Results and Discussion

Irradiating cells with two different pulse repetition frequencies resulted in no statistical difference ($p>0.05$) in SF in all but one sample (H460, 5 Gy, $p=0.0144$), as is shown in Figure 2.2. The presence of the outlier did not warrant further investigation since the discrepancy was not found in the other two cell lines and is small enough to be attributed to experimental inconsistencies. The statistical comparison of samples in filtered and FFF groups (Figure 2.2) indicated no significant difference ($p>0.05$) in all but two samples; H460, 5 Gy, $p=0.0253$ and V79, 10 Gy, $p=0.0377$. Owing to the stochastic nature of cell radiation damage leading to lethality, the differences in survival are deemed accidental. Such differences may have been caused by cell cycle variability, or cell aggregation during treatment, as well as altered metabolic status and oxygenation levels caused by concentrating a large number of cells in a volume of media not optimal for survival.

Figure 2.2 Clonogenic cell survival for varying MU rate and dose per pulse

Cell survival for (a)SiHa, (b)H460 and (c)V79 cells following irradiation at two different MU rates and in filtered and FFF mode. Legend refers to parts a), b) and c)

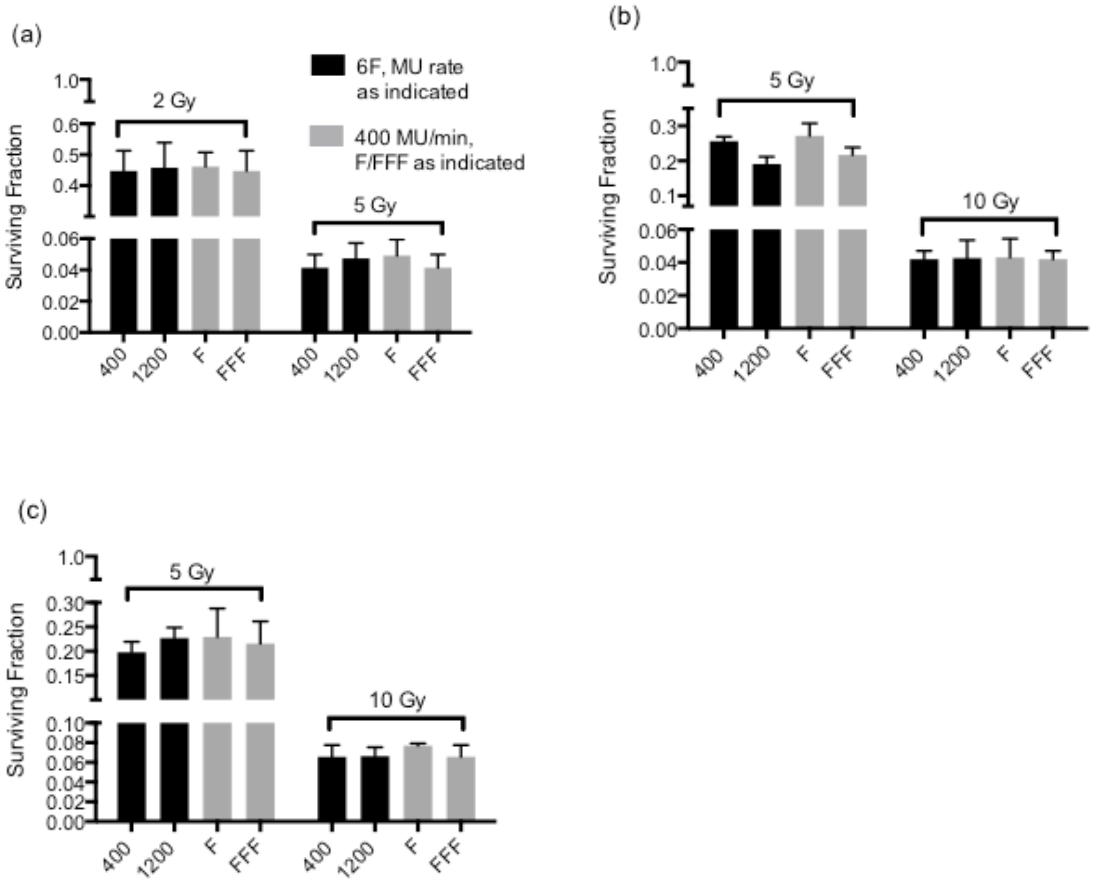

The split-dose data indicated no notable differences between filtered and FFF treatment in the two cell lines, regardless of the time course by which the 10 Gy was delivered as seen in Figure 2.1. A significant ($p<0.05$) increase in survival was seen in the less resistant cell line, H460 for both filtered and FFF beams once dose was protracted to 15 minutes or more rather than delivered in a single beam-on time.

Figure 2.3 Clonogenic cell survival for protracted radiation experiments

Cell survival for (a) H460 and (b) V79 cells following radiation in filtered and FFF modes at a constant MU rate. Treatment delivered acutely or in one of three protraction schemes, as shown in Fig. 2.1

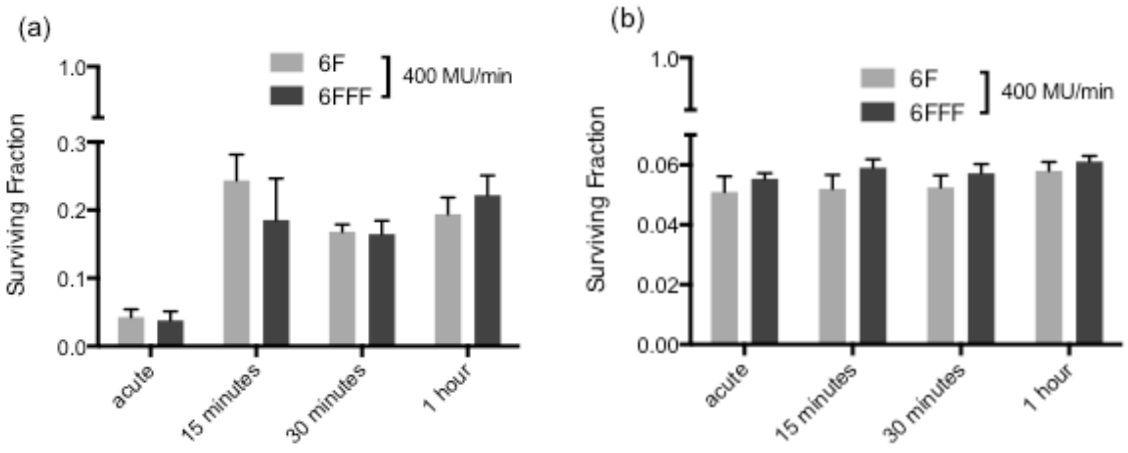

The number of induced and persisting DNA double strand breaks following filtered and FFF radiation treatment was determined by assessing γH2AX fluorescence 1 and 24 hours following radiation treatment, as seen in Figure 2.4.

Figure 2.4 γH2AX staining for cells irradiated in filtered and FFF mode

H460 cells stained with Dapi (cyan), a nuclear marker and γH2AX, which indicates double strand breaks, seen as magenta foci in below images. No differences in the amount of DSBs is seen following 10 Gy of radiation in (a) filtered and (b) FFF photon mode. Scale bars indicate 20 μm.

(a) (b)

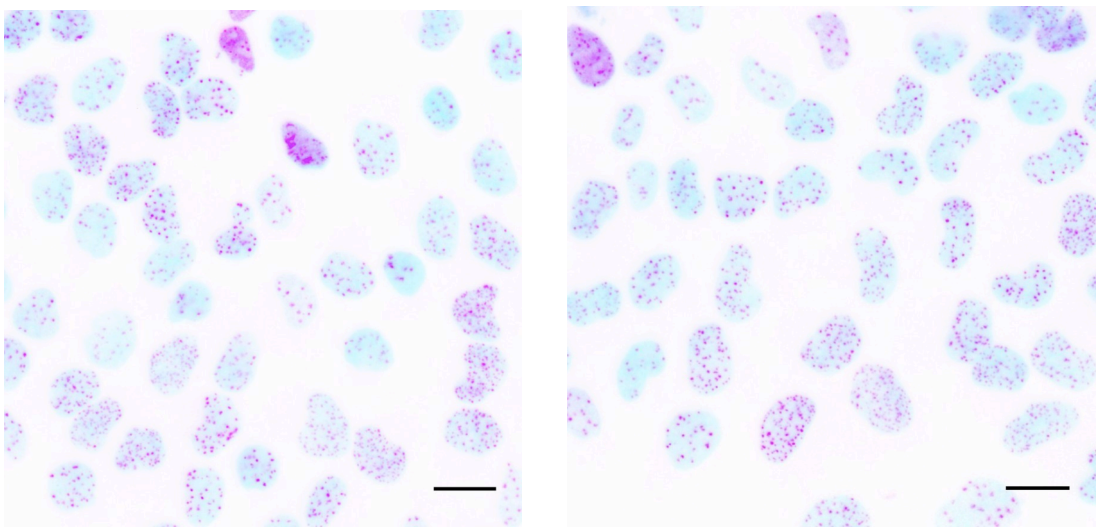

The assay indicated no significant difference ($p > 0.05$) in the induction of DSBs at the 1 hour or 24 hour time points (Figure 2.5). A decrease in overall fluorescence is seen at 24 hours due to the repair of sublethal lesions. The DSBs persisting at 24 hours following radiation treatment are complex to repair and have been suggested as lethal to cells (89). The results are in agreement with the colony assay and imply that an increase in instantaneous dose rate via filter removal at 6X does not result in a greater amount of cell damage or less survival.

Figure 2.5 Quantification of γH2AX fluorescence

γH2AX fluorescence (arbitrary unit) per nucleus of H460 cells 1 and 24 hours following 10 Gy delivered in filtered and FFF modes. Error bars show standard deviation.

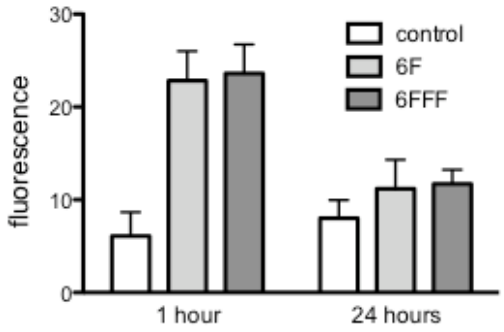

The results imply that increasing instantaneous dose rate does not have an effect on cell survival. Sorensen *et al* showed that survival of V79 and FaDuDD, human head and neck carcinoma cells is independent of instantaneous dose rate. The results of this study are in agreement with those of Sorensen *et al*. It is confirmed that V79 survival is not altered by instantaneous dose rate, and further that H460 and SiHa cells respond in the same manner. The discrepancy in the survival results of previous studies may be due to differences in cell lines and cell cycle synchronization. Lohse *et al* used two human glioblastoma cell lines, and even noted that the response to DPP increase was different in the two lines. Though it was shown that there are no radiobiological effects directly associated with the removal of the flattening filter there remains an advantage in decreasing treatment time by increasing instantaneous dose rate. Generally treatments take 15–45 min, but an increased instantaneous dose rate would enable larger doses to be delivered over a given fraction duration, perhaps having positive implications in tumor eradication.

3 Gated Radiation Planning

Following the confirmation that an increase in instantaneous dose rate does not decrease cell kill while reducing beam on time, the study progressed to gating. Though the preliminary dose rate experiments were done with 6 MV photons, it was felt that 10FFF photon beams would provide the greatest benefit since the maximum output at this energy is 2400 MU/min whereas 6FFF mode offers a more modest increase in MU rate. The gating study began at simulating respiratory traces on a phantom to acquire realistic 4D CT images. Thereafter the CTs were used to plan gated and nongated treatments, which were carried out on a Varian TrueBeam linear accelerator, as seen in workflow Figure 3.1.

Figure 3.1 Workflow for 4D treatments

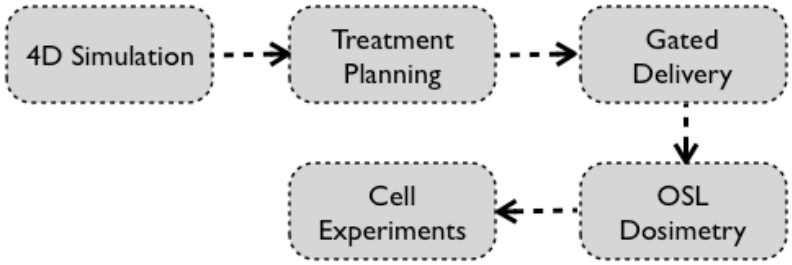

3.1 Overview and limitations

The biggest limitation in a study that aims to improve outcomes in a clinical setting is the likeness of the model to an actual patient. Although the phantom does simulate a real patient's respiration pattern, it only does so in the superior-inferior direction, simplifying the actual rotational motion of the liver during respiration. Seeing as the magnitude of the sup-inf motion is much larger than the anterior-posterior motion due to the nature of diaphragm anatomy, it can be assumed through simplification that the ant-post movement is negligible. The dose calculating algorithms facilitated by CT images consisting of Hounsfield Units ensure that little discrepancy is found between delivering dose to an actual liver rather than an acrylic cylinder. Understandably, however, the precision of the model is compromised due to a lack of

physiological processes, which make delivering doses to patients more difficult. Aside from omitting the immune response of surrounding tissue in radiobiological processes, a phantom faces dosimetric difference as well. For example, if a liver treatment beam is, by chance, being delivered through the lungs respiration will not only change the location of the liver but it will change the volume of air in the lungs altering the liver dosage. Such issues are foreseen drawbacks of a phantom, which is in any case used for studying a sole effect such as the movement of an organ during radiation therapy.

The second limitation is that we are assuming the sup-inf motion of a model liver tumour by use of a surrogate marker placed on top of a phantom, or in a clinical setting, the patient's chest. To measure the usefulness and downfalls of our infrared marker based systems, the alternatives must be examined more closely. An increasingly popular alternative to surrogate tracking for intrafraction tumour movement detection is the use of fiducial markers. These markers are generally made of gold, a biocompatible material, and commonly have dimensions of 1 mm diameter, 5 mm length (90). Amorphous silicon flat-panel detectors which are a common feature of most linear accelerators are used to acquire portal images for use in localization of the markers. The advantage of such fiducials is positional information of the precise object of interest as opposed to a surrogate, which tracks the motion of a related organ (91). Unfortunately, fiducial markers have been shown to move from treatment to treatment (92, 93). Furthermore, while fiducials provide the localization of internal anatomy, it is impossible to attain real time motion with this method because of the increased complexity of image production and registration. There is likewise extra dose to the patient due to the extensive imaging during simulation and treatment.

An alternative to radiographic fiducials are radioactive markers. The implanted marker is tracked via collimated sensors that are mounted onto the gantry, so no external set up is needed from one patient to the next. With a 250 μm diameter, the radioactive markers are much smaller than their radiographic counterparts causing less stress to surrounding tissue during implantation. Unlike other fiducials, the radioactive ones remain static within tissue, thus only a single implant is required for accurate localization of the region of interest. The implants are compatible with X-ray, CT and MRI imagers. Once again, the clear disadvantage of this tracking system is the extra dose to the patient due to the radioactivity of the marker. Furthermore, radioactive markers cannot be effectively used when patients are treated with beam

energies of 10 MV and higher because neutron production yields photons interfering with the marker signal (94).

A third alternative to extraction of internal motion information is the use of a rigid anatomy, such as bones in the vicinity of a target to gauge its motion. The final method discussed is the one employed in this study; respiratory tracking by use of an infrared marker, and infrared emitting diodes. In general, the infrared tracking system has been reported as having equal or better accuracy than the fiducial-based system (95-98). The primary advantage of the infrared surrogate is non-invasiveness and relative simplicity of the procedure compared to the other tracking methods. The challenge, however, is that infrared markers measure solely the displacement of the chest due to breathing, making this a very simplified version of the liver tumour motion. Often the detected motion of the chest is one-dimensional – in the ant-post direction, a model for the sup-inf motion of the liver itself. Furthermore, different markers are used for imaging and treatment, and there is an unavoidable inconsistency in the physical positioning of the marker on the chest, which adds another level of uncertainty in treatment.

3.2 Respiratory Motion Model

To validate the dose distribution in a moving tumour, a phantom capable of programmable respiratory motion was employed with real patient respiratory data. The moving phantom containing a custom insert was CT scanned resulting in a 4D data set that was used to delineate a target in different phases. For the purpose of dosimetry and radiobiological verification in treatment gating, ModusQA's Quasar^{TM} programmable respiratory motion phantom was used (Figure 3.2). The phantom consists of an acrylic body oval (w=30 cm, h=20 cm, l=12 cm) with two cylindrical openings (d=8 cm) for the drive unit and moving insert. A custom acrylic insert was created to enable irradiating cells enclosed in a vessel of specific dimensions, avoiding air gaps (Figure 3.2). Acrylic was deemed a suitable material for the phantom due to its relative water-equivalence, with its electron density approximately 1.147x that of water (99).

Figure 3.2 Modus Quasar Respiratory Motion Phantom

Phantom shown on CT couch. Custom insert seen on the right side, and infrared reflective marker on the moving stage

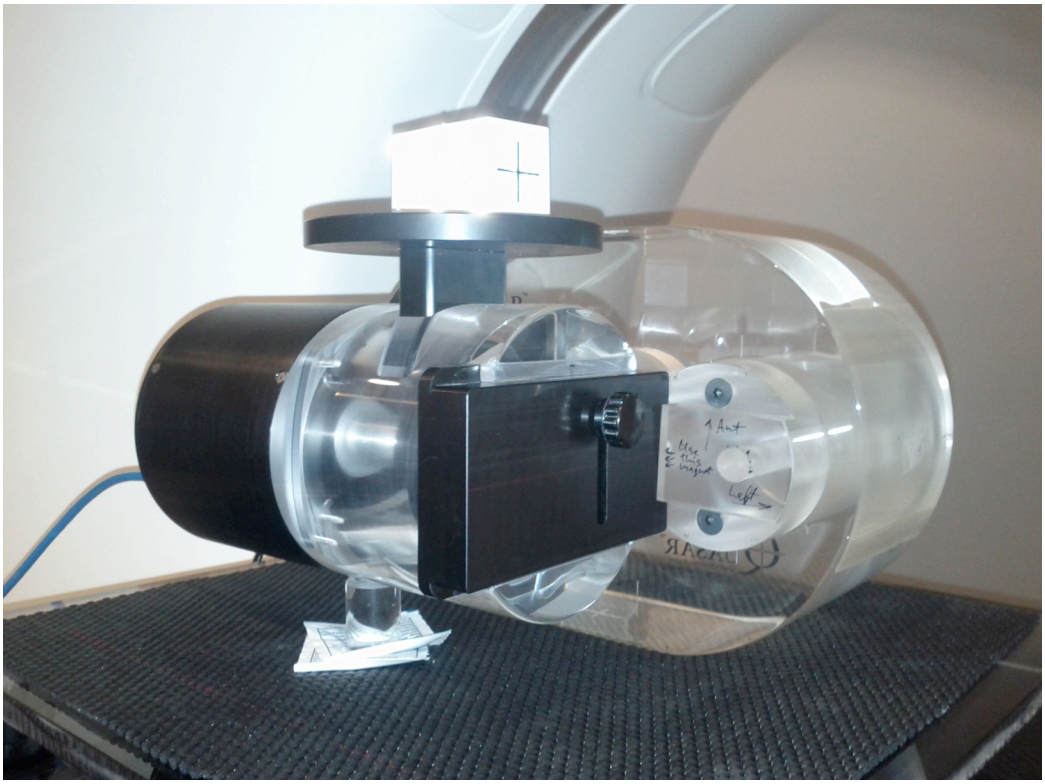

Respiratory traces obtained using Varian real-time position management (RPM) system were imported into the phantom software. The RPM system consists of a reflective marker, which is placed on a patient's chest and illuminated by infrared emitting diodes, and a CCD camera that captures the reflected signal. The camera is connected to a computer and the real-time captured signal is displayed by a software application appearing as a graphical representation. Patient selection was based on treatment site and adequacy of respiratory trace. The traces of 10 patients who had received treatment for liver lesions and who exhibited a fairly regular breathing pattern with no interruptions were selected. The length of the traces varied from 77.60—124.62 seconds or 17-38 respiration cycles. To ensure the traces were sufficiently long for the CT scan and radiation treatment, the available trace was copied and duplicated until a 15 minute trace was achieved. A low pass filter available in the phantom software was applied to eliminate high

frequency noise within the traces. A smoothing function likewise contained in the software was applied, such that any sudden movements requiring high acceleration, which were unable to be processed by the phantom were edited to a manageable form.

As a method of quantifying the periodicity and amplitude variance of the respiratory traces, the data was imported into Matlab for analysis. The infrared marker stage has a direct relationship to the movement of the custom insert, so all amplitude data for the marker was converted into insert motion. A low pass filter with coefficients equal to the reciprocal of the data span was applied to eliminate local maxima and minima (Figure 3.3) and the peaks and troughs were computed by change in slope. A period (or respiratory cycle) was deemed the average duration between two peaks and two troughs. The mean amplitude shown as a straight line in Figure 3.4 was computed as an arbitrary point from which to measure variability in amplitude. A parameter encompassing the combined effect of the period and amplitude of a respiratory trace was defined as the breathing motion speed, as described by (100). The formula is an adaptation of circular motion represented graphically as a sinusoidal wave, and it states that wavespeed is a product of the angular frequency and amplitude ($v=\omega r$), where angular frequency, $\omega=2\pi f$. The wavespeed value becomes an important factor in the interplay effect, as will be discussed in chapter 5. The data is summarized in Table 3.1 for each respiratory trace.

Figure 3.3 A typical respiratory trace

Unfiltered respiratory trace (7) with amplitude of an arbitrary baseline shown on the y-axis.

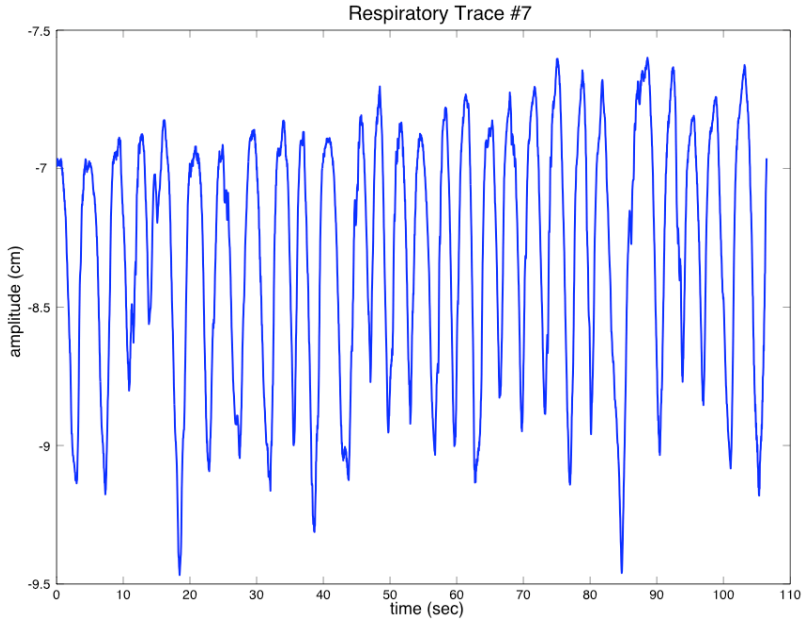

Figure 3.4 Processed respiratory trace

Above respiratory trace (7) following smoothing with a low pass filter and analyzing for points of maximum expiration and inspiration. The average position shown as a black line, with the exhalation and inhalation peaks marked with red and black circles, respectively

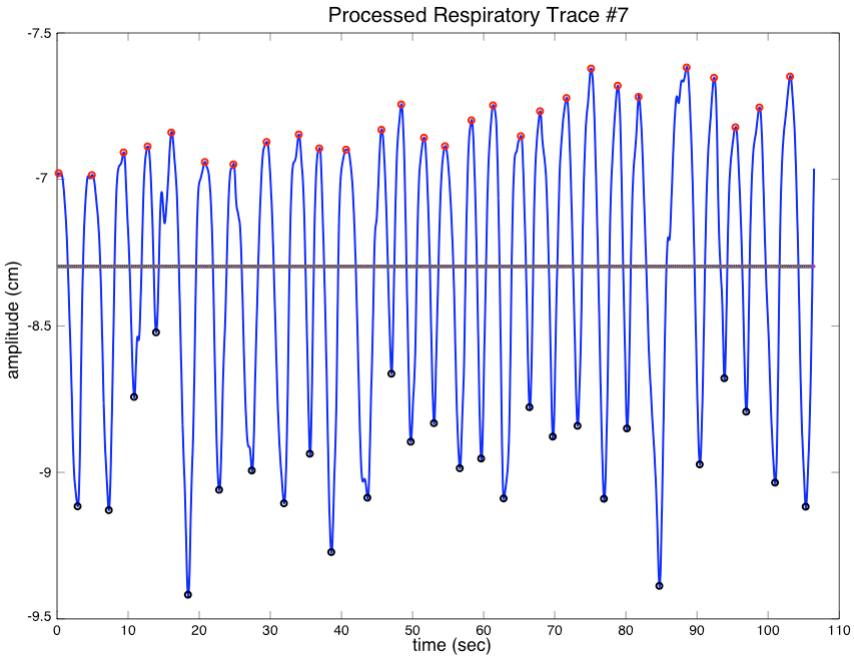

Table 3.1 Summary of respiratory trace characteristics

Respiration parameters attained by Matlab analysis as described in section 3.1.

Trace ID	duration (sec)	duration (cycles)	PTT amplitude (cm)			period (sec)			v (=wr) (cm/s)
			mean	SD	% SD	mean	SD	% SD	
1	77.6	17	0.85	0.40	47.6	4.43	0.77	17.4	1.21
2	124.6	38	0.86	0.41	48.0	3.22	0.45	13.9	1.67
3	91.2	19	0.70	0.43	61.4	4.75	0.58	12.1	0.93
4	90.8	28	0.25	0.28	109.1	3.10	1.17	37.9	0.51
5	83.2	27	0.46	0.31	67.9	3.08	1.83	59.3	0.94
6	100.6	32	0.54	0.21	38.5	3.11	1.09	34.9	1.08
7	106.5	28	1.51	0.45	29.9	3.80	0.80	21.2	2.50
8	101.4	34	0.56	0.33	58.2	2.89	0.72	24.8	1.23
9	106.3	37	0.31	0.18	56.8	2.76	1.05	38.1	0.70
10	106.9	23	0.73	0.27	37.0	4.58	1.82	39.9	1.01

3.3 4D CT Scanning

3.3.1 Background

The motion of the diaphragm during a respiratory cycle causes changes in the geography of most tissue in the thoracic region (Figure 3.5). Various methods are available for use in computed tomography imaging that account that the location of the anatomy will vary with respiration. The first distinction occurs in the manner in which respiration is monitored. Numerous methods are available and require different degrees of invasive procedures, as discussed above.

Figure 3.5 Effect of diaphragm on motion of liver

Left image shows sup-inf motion of diaphragm in a respiratory cycle. On the right diagram, black percentage labels show physical locations of the liver at maximum inspiration (0%) and expiration (50%). Coloured labels show inspiration (0%) and expiration (50%) taken from a common baseline – the mean position.

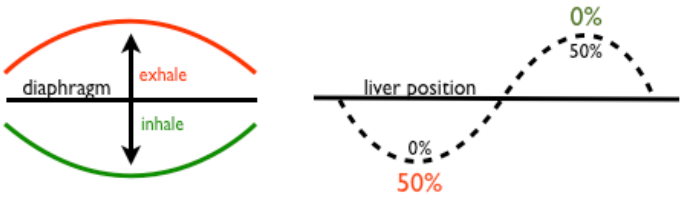

Another variable in 4DCT is the method of gating – prospective or retrospective. The former refers to tracking a patient's respiratory trace, and selecting a part during which you wish the CT to operate – in this way the images are acquired during the select phase where the location of tissue is well known. Retrospective gating refers to running a CT continuously while also tracking a patient's respiration, thus time-stamping each CT slice later to be correlated with a known part of the respiratory cycle. In retrospective gating, images are phase-binned and alike bins used to reconstruct a 3D image.

3.3.2 Method

The acquisition of CT images in different parts of the respiratory cycle requires a method of evaluating the position of a region of interest or a closely related anatomy. The RPM system was used, with the infrared marker placed on the motion stage of the phantom. Initializing the system requires the operator to track a patient's breathing for some cycles, to establish the maximum and minimum positions and the scale for the graphical representation, as well as an estimation of the respiratory period. An algorithm within the system ensures that the breathing is regular in time (101).

The CT scans were done on a GE LightSpeed RT16 CT simulator, in cine mode with 16 detector rows and 8 images per rotation. The cine duration was the respiratory period estimated by RPM plus 1.5 seconds allowing for table advancement. This allowed for a 0.20 second cine time between images and a

slice thickness of 2.5 mm for the best possible image quality, while not overheating the X-ray tube. The time stamps on the CT images and the amplitude and phase information provided by the RPM tracking system were used to collect images from like phases, and use them in phase reconstruction of the 4D image set. In addition to acquiring 4DCTs, the static phantom was scanned using a thoracic protocol, likewise with a 2.5 mm slice thickness.

3.4 Treatment Planning

General Electric Advantage Workstation 4D software was used to phase reconstruct the ten 4DCT images – where 0% corresponds to maximum inhalation and 90% corresponds to maximum expiration (Figure 3.5). The phase CTs, as well as the average intensity projection images consisting of the CTs from phases of corresponding gating windows were exported for dose calculations. The three gating windows chosen for the study were gate 1: 80-20%, gate 2: 40-60% and gate 3: 30-70%, as seen in Figure 3.6. The dose calculation for the nongated treatment was calculated on an average intensity projection image created from all ten phase images.

Figure 3.6 Gating windows used in study

Simplified respiratory trace in diagrammatic form, with 0% phase indicating maximum inhalation and 50% maximum exhalation. Three gating windows used for all experiments are shown in colour.

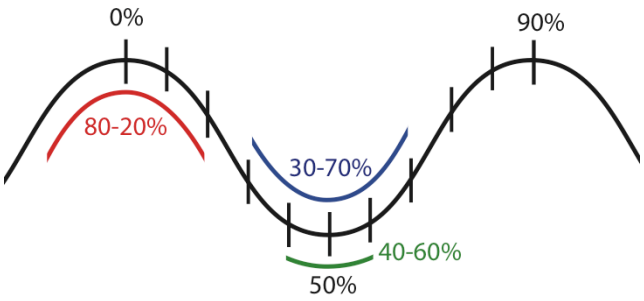

3.4.1 Contouring and External Beam Planning

A phase image is a set of 3D images reconstructed at discrete parts of a respiratory cycle. 4D planning can be done on the 4D image set by establishing a structure on one phase image and propagating it onto the other images. The contour in each individual phase image will have a different location dependent on how much of an effect respiration has on the imaged anatomy. 4D target volumes are created by merging 3D contours from different phase images into a single structure. These '4D' volumes can be used to set optimization parameters in place of 3D structures. The phase images which are used to optimize a plan correspond to the respiratory phases in which the radiation beam-on will occur.

The 4D CT image sets were imported into *Eclipse*™ Treatment Planning System (*Varian* Medical Systems, Palo Alto, CA) equipped with gated 4D planning functionality. The GTV was defined and contoured as the vessel to be used to hold cells and Optically Stimulated Luminescence Dosimeters (OSLDs), while the PTV was contoured as the GTV with a 0.5 cm isotropic external margin for microscopic disease. The cylindrical insert that moves during gating was contoured and designated as the 'liver' organ to approximate dose to normal tissue when PTV dose requirements are met. Finally, the complete body oval was selected as the 'body' and a couch structure was added, namely 'Exact IGRT' Couch Top of medium thickness. All contours were copied to all phases of the respiratory cycle and adjusted accordingly. Since contours were done separately for each respiratory trace, some discrepancies in size occurred, as seen in Table 3.2 which summarizes the mean volume and standard deviation of each contoured object. Composite PTVs, maximum intensity projection (MIP) structures created from the PTVs of each gating window ($PTV_{80\text{-}20\%}$, $PTV_{40\text{-}60\%}$, $PTV_{30\text{-}70\%}$, $PTV_{all\text{-}phases}$) were created as dose targets using the system's 4D structure merge functionality. Numerical validation established that the resultant structures are equivalent to an internal tumour volume created as a MIP of the GTVs in a gating window, with an isotropic 0.5 cm margin for a PTV.

Table 3.2 Summary of contoured volumes

Mean and discrepancy of volumes contoured for the 10 different respiratory traces.

Structure	Mean vol ± SD (cm^3)
GTV	5.64 ± 0.42
PTV	20.28 ± 1.44
liver	530.7 ± 6.55
body	6175.87 ± 104.34

Figure 3.7 3D and transverse views of contoured phantom

Respiratory motion phantom in a 3D (below) and transverse (right) view. Grey is phantom body, blue is the contoured GTV, red is the PTV and yellow (shown outlined on the right) is the 'liver' model. The magenta is a contour of the couch which the phantom is situated on during treatment – Exact IGRT medium thickness couch top.

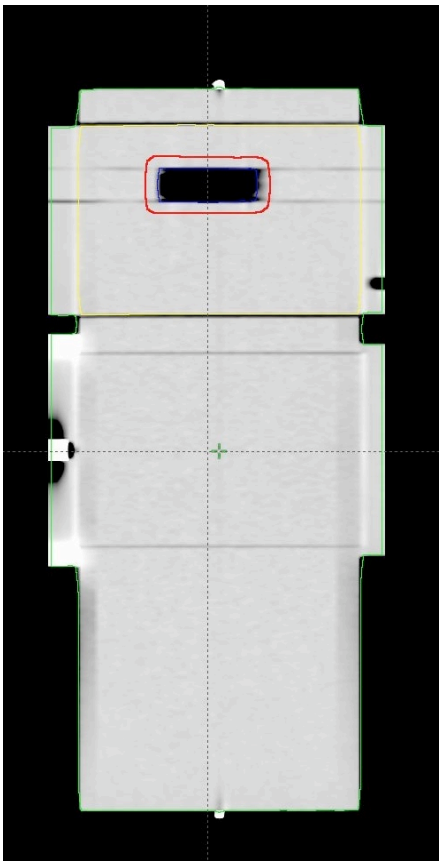

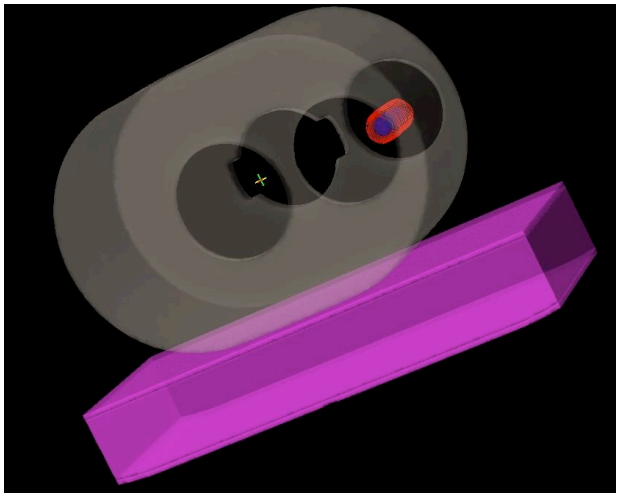

External field beam planning was also carried out in Varian's Eclipse platform. The Anisotropic Analytical Algorithm (AAA) was used to optimize the treatment plan, due to its previous validation for use with FFF beams as published by Hrbacek *et al.* (102). Plans were created for RapidArc with MLC in 10FFF mode, with the gantry rotating from 180 to 315^0 and no further to avoid collision. The collimator field size used was X=10, Y=10 cm with symmetric jaws for consistency though the field created by the MLC was

approximately 2x5 cm in size at most. The collimator was rotated to 35° to smear out the tongue and groove effect in IMRT (103, 104). For each respiratory trace, planning was done for a nongated plan and for the three gating windows. Optimization was carried out using the AAA, with a calculation grid resolution of 2.5 mm. The optimization objectives were as follows:

Minimum PTV dose > 95%

Maximum PTV dose < 115%

Average PTV dose > 95%

Maximum dose being constrained to the PTV

No constraints were placed on dose to the mock 'liver' contour or the total dose to the body since the intent of the study was to solely look at dose to the target. Additionally, a nongated plan was created for the stationary phantom, with the same optimization guidelines. A sample DVH is shown in Figure A.1. The total calculated dose for each of the traces and the static phantom is summarized in Table 3.3.

Figure 3.8 Visualization of field in Eclipse Treatment Planning

Phantom with beam as shown in Eclipse External Planning Software. A 10x10 cm field with MLCs is used in a dynamic 180-315º arc to treat the PTV within the 'liver' (yellow contoured cylinder)

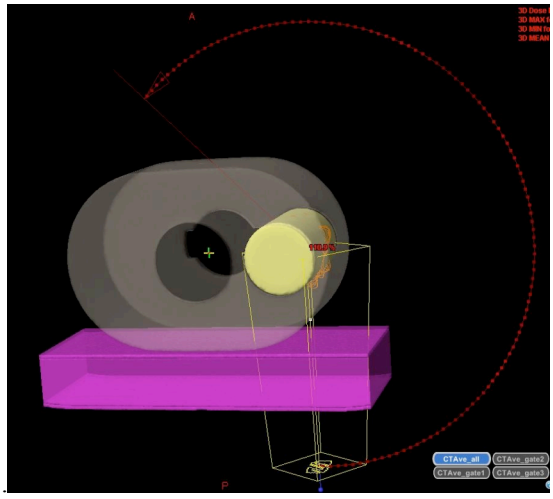

Table 3.3 Eclipse dose statistics for all plans

Summary of doses following VMAT optimization in Eclipse. Doses in % of prescribed (1000 cGy).

trace ID	gating	MU	dose to PTV (% of prescribed)		
			min	max	mean
1	*nongated*	2204	100.1	108.9	104.5
	gate 1	1714	101.0	108.1	104.5
	gate 2	1773	97.1	113	104.6
	gate 3	2120	99.1	110.8	104.9
2	*nongated*	2173	99.4	110.2	104.1
	gate 1	2119	100.3	109.2	104.4
	gate 2	2206	98.1	110.9	104.7
	gate 3	2106	100.0	113.4	104.5
3	*nongated*	2166	98.3	110.0	104.7
	gate 1	1824	100.6	108.8	104.6
	gate 2	2106	97.4	109.2	104.6
	gate 3	2124	100.3	109.9	104.5
4	*nongated*	1899	99.5	110.1	104.6
	gate 1	2161	99.1	109.3	105.0
	gate 2	2078	100.0	109.4	104.7
	gate 3	2151	99.9	109.0	104.6
5	*nongated*	2141	99.7	109.9	104.8
	gate 1	1890	100.5	110.5	104.8
	gate 2	2125	100.8	109.0	105.2
	gate 3	2087	100.1	110.7	104.9
6	*nongated*	2184	100.5	109.4	104.7
	gate 1	2180	99.9	110.0	104.8
	gate 2	2095	100.0	109.5	104.4
	gate 3	2135	99.6	108.9	104.8
7	*nongated*	1847	99.1	110.9	104.5
	gate 1	2158	99.3	109.9	105.0
	gate 2	2180	97.3	109.3	104.6
	gate 3	2132	99.5	109.7	104.9
8	*nongated*	1893	98.3	110.9	104.8
	gate 1	1738	98.8	109.4	104.3
	gate 2	1802	98.4	109.8	104.7
	gate 3	1771	99.0	109.1	104.6
9	*nongated*	2185	98.1	109.8	104.3
	gate 1	2087	99.2	108.8	104.5
	gate 2	2084	99.8	109.7	104.4
	gate 3	1694	97.6	110.3	104.3
10	*nongated*	2143	100.2	109.8	104.5
	gate 1	2209	99.2	109.4	104.5
	gate 2	2163	99.0	109.3	104.4
	gate 3	2182	97.8	111.0	104.6

Figure 3.9 Dose distribution example for a nongated plan of trace 3

Dose shown in transverse and sagittal views. Green indicates 50% isodose (500 cGy), while red wash indicates 110% isodose. Red contour indicates PTV outline.

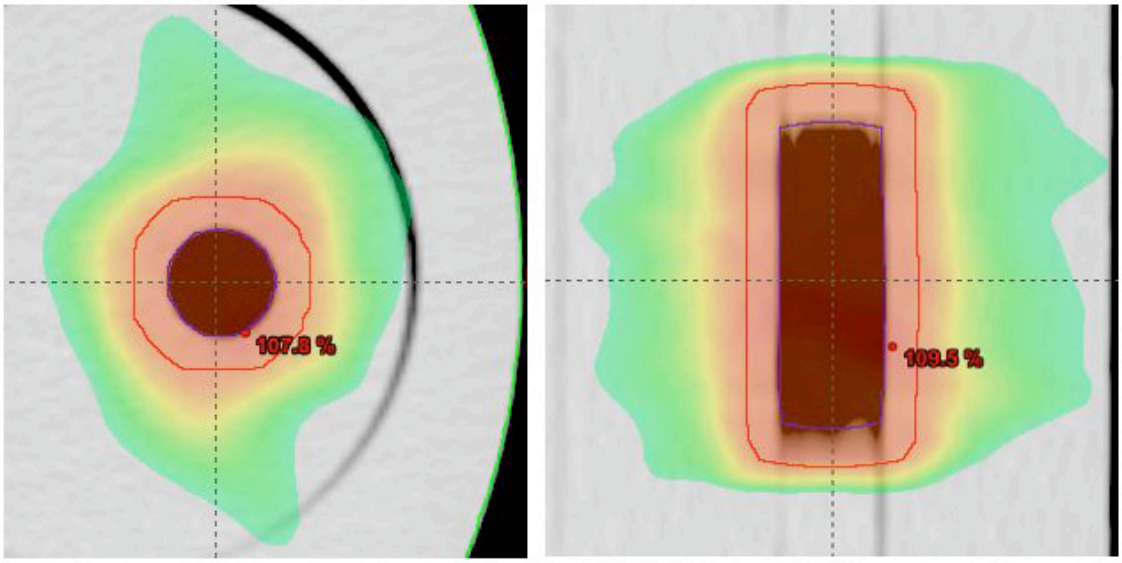

3.4.2 DVH comparisons

The dose-volume histograms (DVHs) produced by Eclipse were compared in several manners. One parameter obtained is the homogeneity index (HI), defined as the difference between the doses received by 2% and 98% of the PTV, thus a lower HI indicates better homogeneity. The gradient measure, the difference between the equivalent sphere diameters of volumes receiving 100% and 50% of the prescribed dose was obtained from Eclipse. The increase in gradient measure implies a less steep dose fall-off, a common attribute in plans involving improved homogeneity (105). The summary of the corresponding indices is presented in Table 3.5.

Table 3.4 Homogeneity index and gradient measure from Eclipse dose statistics. Columns stand for plan type: '-' implies nongated and 1,2,3 correspond to the various gated plans. Rows imply respiratory traces 1-10. Green implies the gated index decreased from the nongated, red that it increased.

	homogeneity index				gradient measure			
	-	1	2	3	-	1	2	3
1	0.046	0.037	0.064	0.051	1.12	1.15	1.07	1.04
2	0.057	0.045	0.052	0.052	1.13	1.15	1.08	1.12
3	0.054	0.041	0.061	0.05	1.19	1.13	1.09	1.12
4	0.05	0.047	0.049	0.044	1.12	1.03	1.14	1.2
5	0.053	0.051	0.040	0.054	1.13	1.16	1.03	1.12
6	0.047	0.045	0.037	0.049	1.13	1.16	1.17	1.13
7	0.058	0.048	0.044	0.048	1.1	1.06	1.13	1.16
8	0.054	0.055	0.060	0.046	1.05	1.13	1.05	1.09
9	0.062	0.048	0.053	0.064	1.1	1.22	1.13	1.13
10	0.055	0.052	0.047	0.059	1.14	1.2	1.14	1.16

3.4.3 Target volume and motion comparison

4D CT scans are often acquired solely for the purpose of imaging a target and surrounding tissues in the extreme parts of a respiratory cycle. In such cases, objects are (generally) contoured in the maximum expiration and inspiration CTs and the target is defined as combination (often a MIP) of the structures in the two extreme CT images. The volumes of contoured objects change distinctly from one respiratory phase to the next, as can be seen for the GTV in this study in Figure 3.10. Furthermore, phase CT images allow the perceived motion as registered by the scanner to be measured. A single part of the vial was chosen in each CT, and its 3-dimensional location recorded. The shift from the baseline (chosen to be the 0% phase image) is shown in Figure 3.11.

Figure 3.10 Volume differences between phase CTs

Differences in volume of contoured GTV for different phase CTs for each respiratory trace.

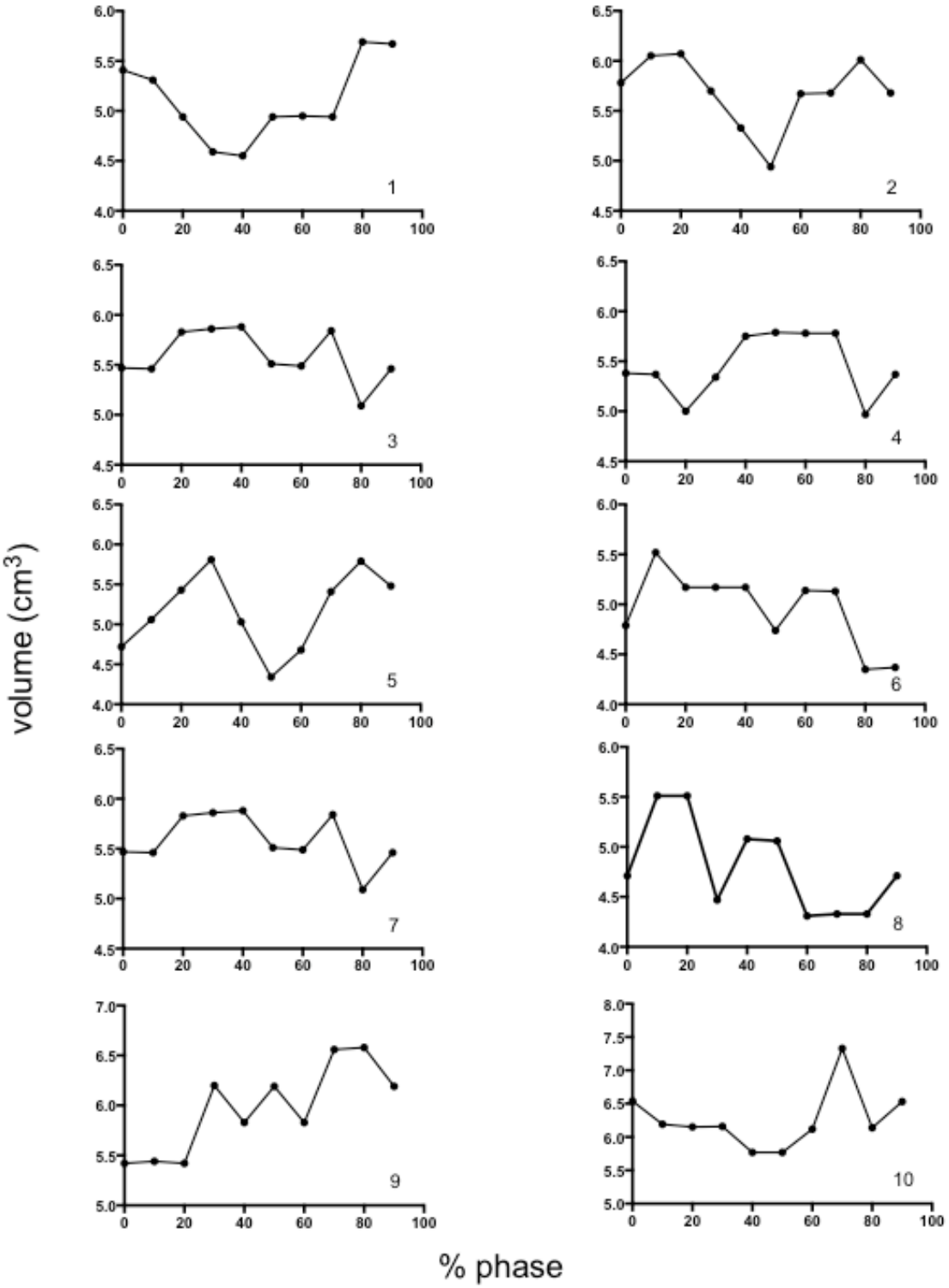

Figure 3.11 PTV motion as observed in phase CTs

Location of PTV in different phase CTs in relation to the 0% CT.

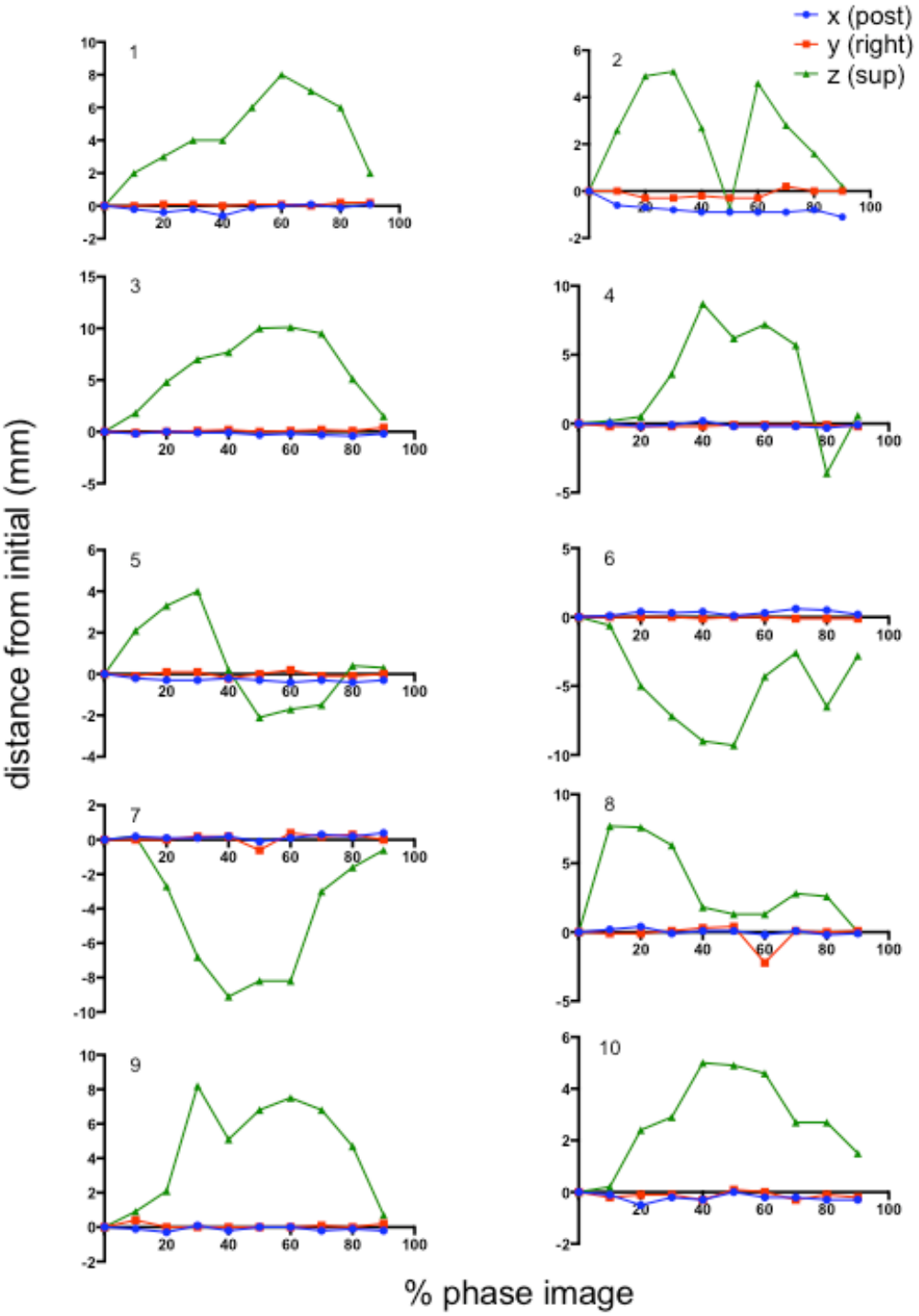

The motion of a diaphragm and the vicinity of the liver by comparison would indicate the motion of a liver tumour would move as shown in Figure 3.11 (3). In two instances - namely for the phase CT images of trace 2 (Figure 3.11 (2)) and 8 (Figure 3.11 (8)), phases 0-90% seem to capture two respiratory cycles instead of one. In these cases the cine duration – the duration for which the images of one respiratory cycle are collected –may have been too long such that what was assumed to be one respiratory cycle was actually two. This may have stemmed from various reasons, one being that a respiratory period is estimated by tracking breathing for a few cycles on RPM, and then making the cine duration ~1.5 seconds longer allowing for table advancement. Interestingly neither traces 2 nor 8 have the largest percent error in the mean period, however the initial part of the traces, when a period was established by RPM may just be much different than the remaining, more uniform trace.

The change in the direction of motion can also be attributed to the change of volume of the vial, as can be seen in Figure 3.10. Both traces 2 and 8 exhibit sharp dips in volume in the 50% phase CT, which are further seen in Figure 3.12. The CT motion was acquired by placing a marker at the top of the vial and tracking its location in each of the sagittal slices of the phase CTs. The location of the marker would therefore be affected if the dimensions of the vial changed in the image, as they did. The change in volume can be attributed to CT reconstruction artifacts. Notably, among the three traces that resulted in changing vial volumes, the common thread is solely a relatively high breathing speed, as calculated previously. The incorrect representation of a cell vial suggests an inadequate amount of data for the reconstruction of the CT images.

In two instances the maximum expiration phase shows the largest negative amplitude – trace 6 and trace 7 (Figure 3.11 (f) and (g)). There was no manual setting for the maximum inspiration and expiration, rather the RPM itself decided upon what it deemed a 0% (maximum inspiration) and 50% (maximum expiration) phase. Though the two instances occurred on the same day, a manual set up error is unlikely since two other CT images exhibit expected behavior.

Though the above mentioned instances would have resulted in completely incorrect contours in terms of duty cycles and gating windows, it seemed to not result in any trend in OSL dosimetry or survival patterns, as will be seen in the following two chapters.

Figure 3.12 Differences in GTV volume in phase CTs

Image taken from Eclipse Treatment Planning System

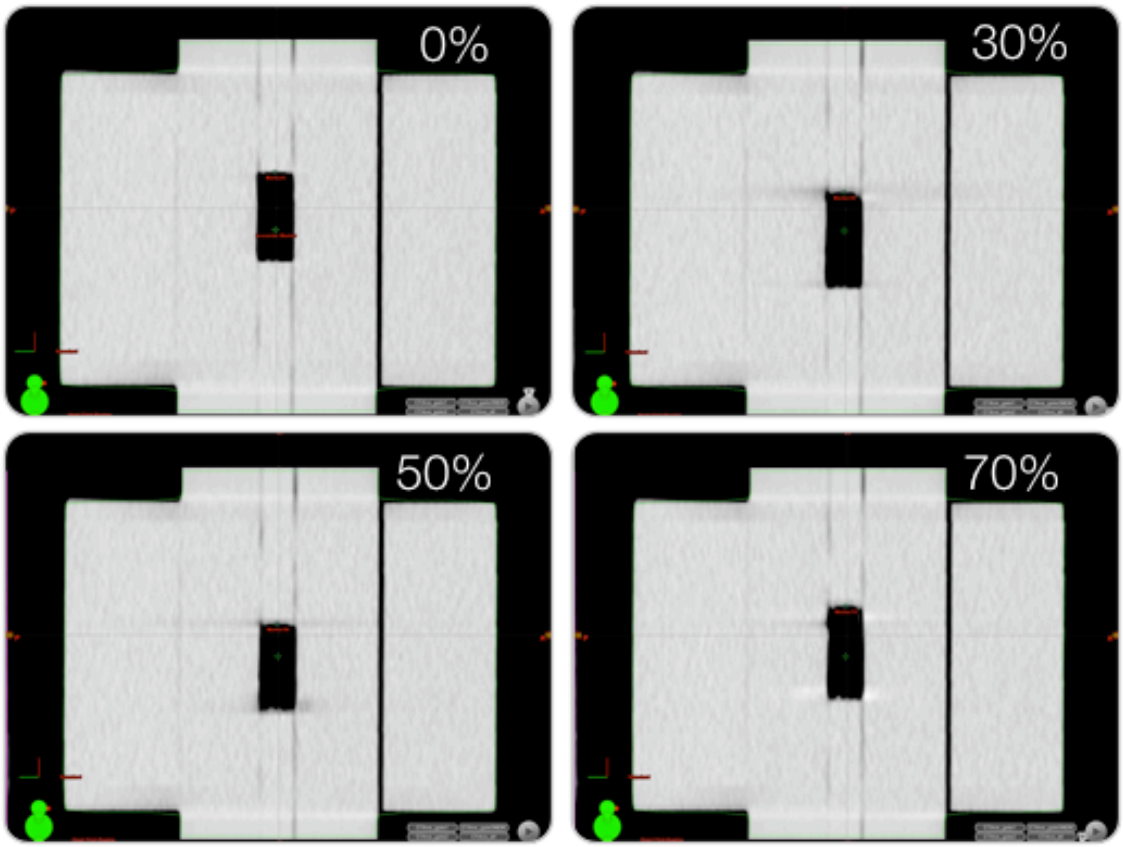

3.5 Linac experiments

Created and approved plans from Eclipse were imported into TrueBeam STx for purpose of treatment delivery. The RPM system was used in amplitude gating mode, and a system of phantom motion tracking was set up in a similar manner as for the CT imaging. The upper and lower amplitude limits were visually determined to correspond to the desired phase gating windows as shown in Figure 3.6, and are summarized in Table 3.5. After the amplitude limits were set for each of the gating windows, the treatments are delivered to dosimeters, or cells as described in the sections that follow. The duration of approximate treatment time is summarized in Table 3.5.

Table 3.5 Summary of treatment duration and amplitude limits for all plans

Treatment duration implying the time between first beam on and last beam off, including pauses in gated treatments.

		Limits (cm)		duration
ID	Plan	Upper	Lower	OSLD (min)
1	*nongated*	-	-	0.54
	gate 1	1	0.3	6.05
	gate 2	0.08	-1	2.40
	gate 3	0.1	-1	2.21
2	*nongated*	-	-	0.54
	gate 1	1	0.12	2.39
	gate 2	0.02	-1	3.53
	gate 3	0.10	-1	1.59
3	*nongated*	-	-	0.54
	gate 1	1	0.08	4.53
	gate 2	-0.2	-1	6.40
	gate 3	0	-1	1.46
4	*nongated*	-	-	0.54
	gate 1	1	-0.1	3.22
	gate 2	-0.2	-1	12.35
	gate 3	-0.1	-1	3.12
5	*nongated*	-	-	0.54
	gate 1	1	0.25	2.43
	gate 2	0	-1	12.35
	gate 3	0.13	-1	3.12
6	*nongated*	-	-	0.55
	gate 1	1	0.2	2.43
	gate 2	0.05	-1	5.34
	gate 3	0.09	-1	3.26
7	*nongated*	-	-	0.54
	gate 1	1	0.25	2.53
	gate 2	0.03	-1	3.12
	gate 3	0.06	-1	2.35
8	*nongated*	-	-	0.46
	gate 1	1	0.25	1.52
	gate 2	0.15	-1	4.03
	gate 3	1.20	-1	2.34
9	*nongated*	-	-	0.44
	gate 1	1	0.05	3.28
	gate 2	-0.20	-1	13.05
	gate 3	-0.10	-1	2.57
10	*nongated*	-	-	0.56
	gate 1	1	0.25	2.52
	gate 2	0.07	-1	6.16
	gate 3	0.12	-1	2.51

Figure 3.13 Gating set up on True Beam treatment unit

A movie of several respiratory traces is used and predicted beam-on times are shown for the 80-20% gating window.

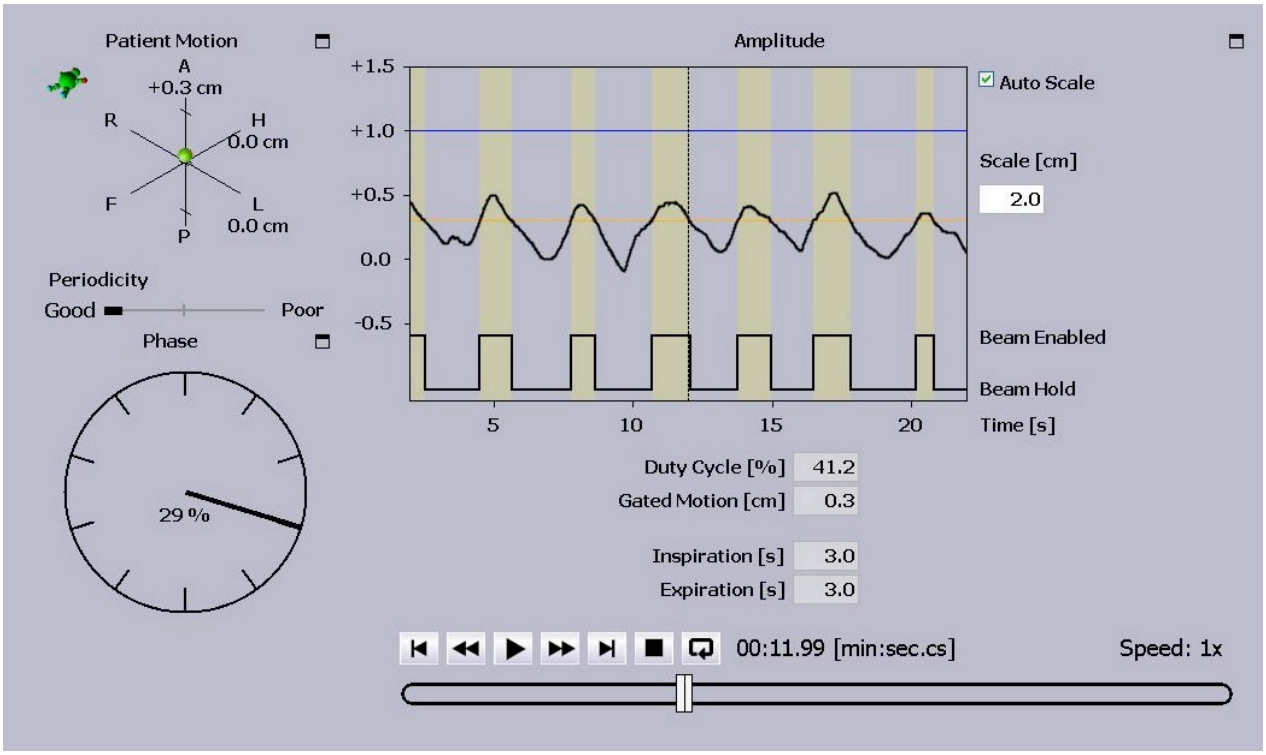

4 Dosimetry

Sensitivity and lack of saturation are the necessary constituents of dosimeters used for purposes of determining the output of linear accelerator for a given planned dose. Tissue (or water) equivalence or lack thereof can be overcome via various conversion factors, but this introduces an outside error that preferably ought to be avoided. When a dose is being delivered by VMAT, dose rate and beam angle independence become a requirement for accurate dosimetry. A linear or easily determined dose-response relationship assures that dosimetry is reproducible and non-ambiguous. Other attributes are those of convenience, including quick and non-destructive read-outs, allowing for multiple measurements with the same dosimeter. Dosimeters that can be used multiple times while still providing accurate dose measurements are economically justified. Each method of radiation treatment has a different optimal dosimeter dependent on, but not limited to photon energy, field size, set-up, and room geometry.

SBRT presents the ultimate challenge in dosimetry of radiation beams - steep fluence gradients, changes in dose-rate and gantry directionality and notably small fields (13). Though there is no clear consensus on what a 'small' radiation field is, Taylor *et al.* (106) state it is generally below 4x4 cm, and Das *et al.* (107) conclude it is a field smaller than 3x3 cm. Dependent on how small of a field a multileaf collimator creates during an arc, a loss of lateral electronic equilibrium may occur (107). The 10FFF photons used in this study have a d_{max} of 2.8 cm for a 10x10 cm field size, thus the secondary electrons may have a range that extends past the field and detector itself. Dosimetric techniques have been compared for stereotactic fields (108) with stress on tissue equivalence, small size and high spatial resolution.

Al_2O_3 suffers from a lack of water-equivalence at kV energies (109), however at MV energies, and in particular at 10 MV, the cross sections of the two materials are much the same and dominated by incoherent scattering (Figure 4.1). The other issue arising with photons of 10+ MV energies is the appearance of neutron-producing photon interactions. ~$2x10^{-7}$ neutrons are produced for every photon incident onto water, tissue or an equivalent material (110). Al_2O_3:C OSLDs have a low sensitivity to neutrons (111) however the contamination is not alarming due to the lack of the FF that contributes to neutron production.

Figure 4.1 Cross section for Aluminum Oxide and water

Cross-sections of water (a) and Aluminum Oxide (b) for the various photon interactions for energies of 0.001-100 MeV. Line at 10 MeV to stress the OSLD-water equivalence at 10X.

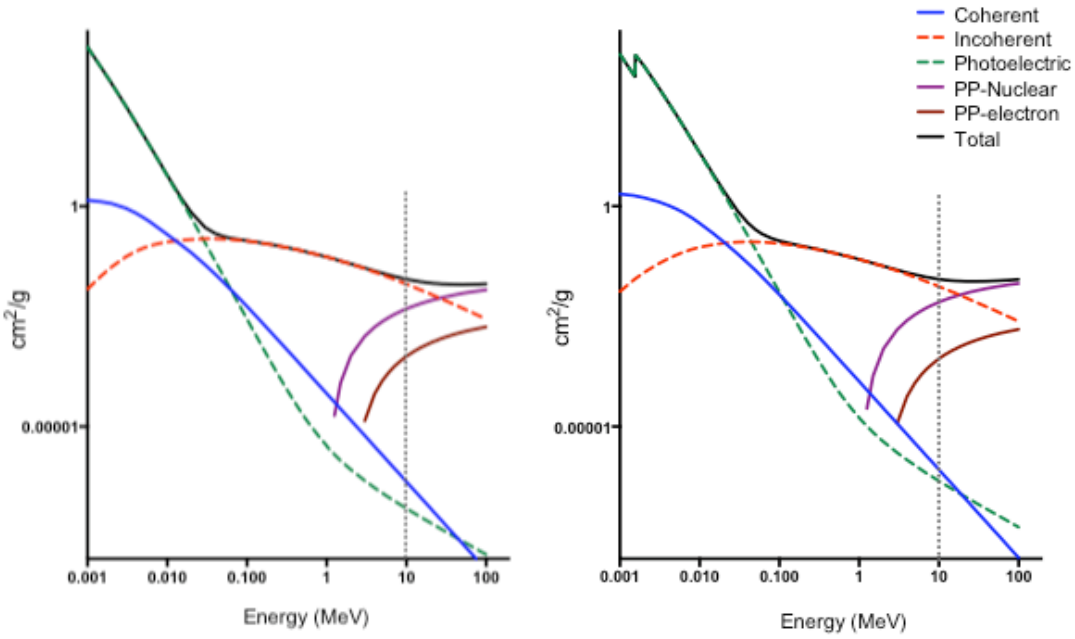

OSL dosimeters have been shown to be virtually independent of dose rate. Aznar *et al.* (112) showed a variation of 0.3% in accumulated dose for OSLDs irradiated with 0.85 cGy at various MU rates for 6 MV photons. VMAT plans have fluctuating dose rates, but this non-significance of dosimeter dose rate dependence ensures a calibration curve with a single dose rate can still be applied. The angular dependence was shown to result in a 1-2% difference in accumulated dose (112) when a beam was normal to the a thin edge of the OSLD disk as opposed to its larger circular surface. Since the experimental plans in this study involved a 180-315° arc while the calibration curve was obtained in a single configuration, this introduces an error, albeit acceptable, in the dosimetry measurements. Importantly, all of the plans in the experiments were delivered as an arc and so inter-experiment comparisons avoid this added error.

The dimension of the dosimeter disk is 5 mm in diameter with a 0.3 mm thickness, providing an overall effective volume of 5.9 mm^3. Using OSLDs minimizes the effects of volume averaging seen in many other standard dosimeters such as the farmer-type ionization chamber with an effective volume of 0.6 cc. Consequently the OSLD being smaller than the PTV indicates areas of inhomogeneity cannot be measured with this dosimeter.

4.1 OSLD Mechanism

Optically stimulated luminescence dosimeters consist of materials of a crystalline structure with imperfections in the lattice, which act as electron trapping sites. Ionizing radiation causes electrons to migrate to the conduction band leaving holes in the valence band. Electrons and holes move around until they recombine or are captured by the trapping sites in the band gap. The dosimetric property of the materials comes from the fact that the trapped charge concentration at such sites is directly proportional to the dose absorbed by the material.

To obtain a luminescence signal proportional to dose, a pulsed or continuous-wave light source (LED, laser) is used to stimulate the recombination of electrons and holes that produces luminescence. The light source is filtered to a certain wavelength, and detection filters block this stimulating light while accepting the OSL signal through. A light detector such as a photomultiplier tube is used to quantify the signal produced. The integral of luminescence produced during stimulation can directly be related to dose (113). During irradiation, low-energy electron traps are filled and thereafter spontaneously emptied with no stimulation. A resting period of 8+ minutes allows for the depletion of the low-energy traps such that they do not interfere with the radiation signal during stimulation (114).

4.2 Methods

A calibration curve was obtained by delivering various doses (10, 100, 300, 500, 800, 1000, 1300 cGy) to groups of 3 OSLDs at a time. The calibration was carried out with a 10MV filter free photon beam with a 10x10cm field size at SSD=100 cm. 17 cm thick solid water slabs were placed below the OSLDs for full back-scattering conditions, and 0.5 cm thick bolus sheet was placed over the OSLD dots and covered

with 2.3 cm thick water slabs. This resulted in the optimal build up effect since the OSLDs were at a depth of 2.8 cm, the d_{max} for 10 MV FFF photons. The MU rate used was the highest available – 2400 MU/min to match the maximum rate in RapidArc planning for the gated treatment delivery. After completion of radiation delivery, the OSLDs were left for 30 minutes allowing for the depletion of low energy traps. *Landauer inc.* microStar OSLD reader with an LED light source was used to perform three readings of each OSLD dot and create a non-linear calibration curve. The microStar program resulted in a second-order polynomial fit with the following parameters, relating the reader signal to dose:

$$\text{Dose} = \mathbf{(-6.021982 \times 10^{-10})}\text{counts}^2 + \mathbf{0.001083966} \times \text{counts} + \mathbf{8.669243}$$

The program used this fit to obtain the dose received by each dosimeter. Repeating the calibration curve fit in Matlab resulted in the following graph, as seen in Figure 4.2.

Figure 4.2 Non-linear OSLD calibration curve

Calibration curve relating photon counts to the absorbed dose for OSLDs irradiated at standard conditions.

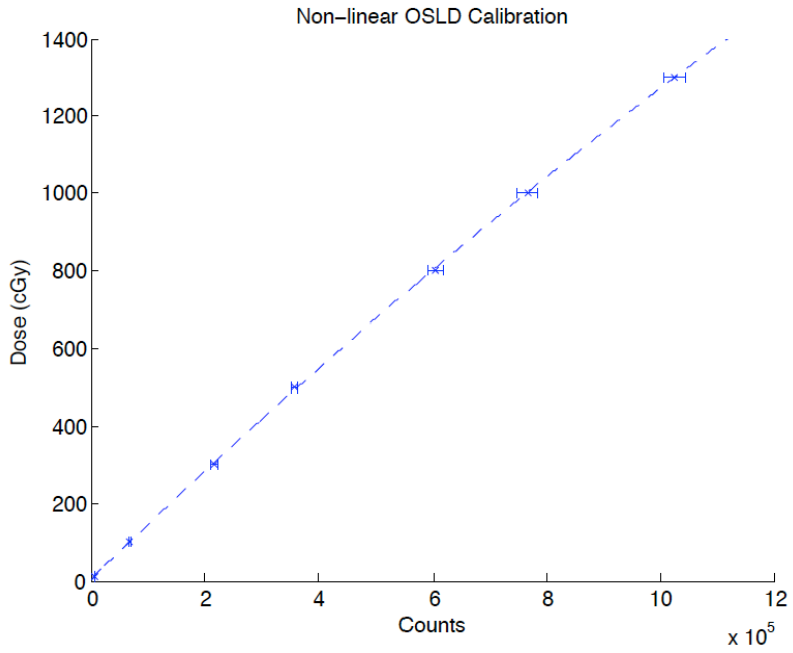

To determine the dose received following each gated and nongated treatment plan, a vessel containing OSLDs was placed into the slot for the PTV and irradiations were carried out as usual. The dose

was obtained by reading the luminescence in microStar and using the non-linear calibration curve to find the dose delivered. Each dosimeter was read 3 times consecutively, so as to have replicate readings while avoiding signal depletion.

4.3 Results and Discussion

Table 4.1 summarizes the doses for each plan as measured by OSL dosimeters. Table 4.2 shows the discrepancy in dose predicted by Eclipse versus the measured dose. The differences in Table 4.2 are normalized to the Eclipse dose to account for discrepancies in the reference dose due to the nature of the Eclipse algorithm. In a majority of the plans (30/40), the dose predicted by Eclipse was larger than the measured dose. Of the 10 plans which showed a converse trend, six were for nongated regimens, indicating a majority (6/10) of nongated plans will result in physically higher doses than predicted by the treatment planning system. The closest agreements between Eclipse and OSLD was observed in plans with a 40-60% gating window (4/10). Two of the plans resulted in dose discrepancies above 4% of the Eclipse dose, with the predicted dose being higher than the physical. In particular the 80-20% gating window plan for trace 8 resulted in a 7.8% difference in planned and physical dose. In Figure 3.11 (h), the phase CT movement analysis indicated the PTV in the 50% phase had maximum negative rather than positive displacement, unlike a majority of the other traces. This may have been the instigator of a dose discrepancy of 7.8% in the plan for the 80-20% gating window of respiratory trace 8. If the contour was done for what was incorrectly thought to be the point of maximum inspiration, the discrepancy in dose may become this large. There was a 1.64% dose difference in the nongated delivery to a static phantom, indicating factors other than phantom motion account for dose inconsistencies. Overall, 24/40 (6/10 nongated, 18/30 gated) plans resulted in planned to physical differences of <2% of the Eclipse dose. 30/40 plans (8/10 nongated, 22/30 gated) had differences of <3%.

Table 4.1 OSLD dose summary

Comparison of OSLD dose accumulation to the planned Eclipse dose.

		osld		Eclipse dose to PTV			
		avg dose	sd dose	mean (%)	SD (%)	mean (cGy)	SD (cGy)
1	gate 1	1013.21	0.711	104.5	1	1045	10
	gate 2	1009.24	6.371	104.6	1.4	1046	14
	gate 3	1017.43	3.648	104.9	1.1	1049	11
	non-gated	1004.43	1.699	104.5	1.1	1045	11
2	gate 1	1015.53	7.107	104.4	1.1	1044	11
	gate 2	1033.48	3.557	104.7	1.2	1047	12
	gate 3	1045.71	1.158	104.5	1.3	1045	13
	non-gated	1052.44	5.970	104.1	1.3	1041	13
3	gate 1	1016.29	2.668	104.6	1	1046	10
	gate 2	1051.38	3.567	104.6	1.3	1046	13
	gate 3	1005.32	2.687	104.6	1.2	1046	12
	non-gated	1048.35	6.941	104.7	1.3	1047	13
4	gate 1	1033.51	2.275	105	1	1050	10
	gate 2	1032.74	13.214	104.7	1.2	1047	12
	gate 3	1062.07	9.399	104.6	1.1	1046	11
	non-gated	1056.85	11.320	104.6	1.2	1046	12
5	gate 1	1030.60	13.65	104.8	1.2	1048	12
	gate 2	1012.06	8.363	105.2	0.9	1052	9
	gate 3	1046.89	13.423	104.9	1.3	1049	13
	non-gated	1025.95	3.764	104.8	1.3	1048	13
6	gate 1	1013.35	14.572	104.8	1	1048	10
	gate 2	1030.81	3.946	104.4	0.9	1044	9
	gate 3	1020.17	6.076	104.8	1.2	1048	12
	non-gated	1002.41	9.175	104.7	1.2	1047	12
7	gate 1	1049.95	5.763	105	1.1	1050	11
	gate 2	1035.29	2.335	104.6	1.1	1046	11
	gate 3	1016.78	1.173	104.9	1.2	1049	12
	non-gated	1052.95	1.678	104.5	1.3	1045	13
8	gate 1	961.64	3.651	104.3	1.4	1043	14
	gate 2	1025.76	0.582	104.7	1.3	1047	13
	gate 3	1025.95	0.466	104.6	1	1046	10
	non-gated	1036.39	1.395	104.8	1.2	1048	12
9	gate 1	1035.77	3.826	104.5	1.1	1045	11
	gate 2	1023.64	2.682	104.4	1.2	1044	12
	gate 3	1045.80	3.492	104.3	1.4	1043	14
	non-gated	1070.88	0.591	104.3	1.4	1043	14
10	gate 1	1032.08	12.835	104.5	1.2	1045	12
	gate 2	1033.59	8.141	104.4	1.1	1044	11
	gate 3	1031.56	7.192	104.6	1.3	1046	13
	non-gated	1065.81	11.914	104.5	1.2	1045	12
static	non-gated	1030.25	2.718	104.7	1.2	1047	12

Table 4.2: Planned to measured dose differences

The discrepancies between the mean PTV dose predicted by Eclipse Treatment Planning System and the dose obtained through OSLD dosimetry (in % of mean PTV dose as calculated by Eclipse). Prescribed dose was 1000 cGy to the PTV, which enclosed the OSLDs. Columns refer to the following gate schemes: 1=80-20% , 2=40-60% , 3=30-70% gating windows.

Trace	$D_{Eclipse}$- D_{OSLD} (% of $D_{Eclipse}$)							
	nongated		1		2		3	
	mean	sd	mean	sd	mean	sd	mean	sd
1	3.88	0.35	3.04	1.05	3.51	1.99	3.01	1.43
2	-1.10	1.67	2.73	1.76	1.29	1.50	-0.07	1.35
3	-0.13	14.72	2.84	1.24	-0.51	1.58	3.89	1.45
4	-1.04	2.16	1.57	1.18	1.36	2.42	-1.54	1.93
5	2.10	0.79	1.66	2.47	3.80	1.68	0.020	2.52
6	4.26	0.52	3.31	2.38	1.26	1.25	2.66	1.76
7	-0.76	1.85	0.00	1.60	1.02	1.29	3.07	1.29
8	1.11	1.17	7.80	1.80	2.03	1.32	1.92	1.02
9	-2.67	0.56	0.88	1.43	1.95	1.43	-0.27	1.67
10	-1.99	1.17	1.24	2.39	1.00	1.84	1.38	1.95
static	1.64	0.57						

The OSLD measurements, normalized to the Eclipse mean PTV dose are shown in Figure 4.3. The error bars represent standard deviation arising from the three OSLD readouts and the error in the mean PTV dose as indicated by Eclipse. Asterisks emphasize a statistically significant difference between the dose for each gated plan and the nongated plan of the same trace. Table 4.3 contains the p-values for all groups.

The largest dose for a respiratory trace was most often that of a nongated plan (5/10). There was no particular trend in the plans receiving the smallest dose. A particularly notable decrease in the physical dose is seen for trace 8, 80-20% gating window, also the plan corresponding to the largest planned to physical dose difference.

25/40 of the plans (7/10 nongated, 18/30 gated) had planning system to measured dose discrepancies smaller than 2%. The differences were <3% for 30 of the 40 plans (9/10 nongated and 21/30 gated). The differences of approximately 30 cGy are not associated with biologically significant consequences. As seen in Table 3.4, gated plans show an improved homogeneity with the tradeoff being a

worsening of the gradient effect. The issue of the finite dosimeter volume remains, as the point dose measurements could not effectively account for all inhomogeneity within the larger PTV volume.

The larger doses are seen in the nongated plan and the plan with the longest duty cycle. This is expected as in both the cases, the composite PTV target contour encompasses the insert in all extents of its motion. A further factor in the differences between Eclipse and OSLD doses may be the disparity in 4D image reconstruction and the method of gated treatment. Periodic respiration with varying amplitude will result in similar images in phase and amplitude binning. Nonperiodic respiration with a constant amplitude will, however, result in large differences between the two methods (115). A target is contoured in a phase-reconstructed image, while amplitude-based gating is applied during treatment, such that if the time-weighted motion is different, there will be inconsistencies in dose.

A further factor in dosimetric differences may be the interplay effect discussed in the following chapter as it likewise pertains to cell survival.

Figure 4.3 OSLD dose comparisons

Doses obtained by OSLD dosimetry for each respiratory trace, identified by a dashed line. Each dose was normalized to the mean PTV dose as calculated by Eclipse. '-' implies the treatment was nongated, while the other groups are for gated treatments with the following gating windows: 1=80-20% , 2=40-60% , 3=30-70%. The last bar, indicated by 's' implies the measurement was for a static phantom.

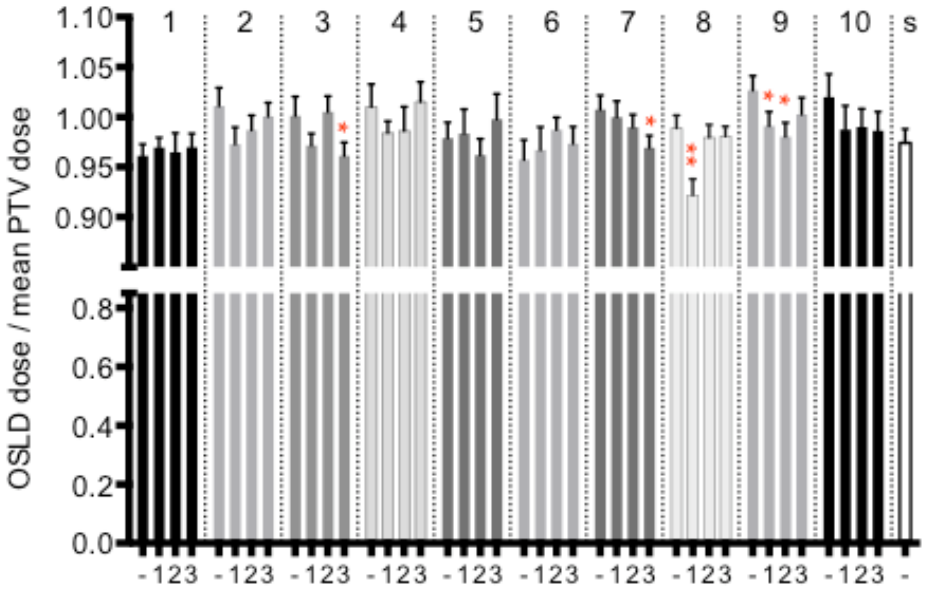

Table 4.3 OSLD p-value summary

P-values for above graphs, comparing OSLD doses of gated plans to their nongated counterparts.

Trace	1 vs -	2 vs -	3 vs -
1	0.3996	0.7925	0.4497
2	0.0576	0.1566	0.4810
3	0.0967	0.8019	0.0466*
4	0.1714	0.2740	0.7863
5	0.8057	0.2639	0.3399
6	0.6172	0.1026	0.3474
7	0.5680	0.1793	0.0246*
8	0.0054**	0.4240	0.4339
9	0.0376*	0.0160*	0.1344
10	0.1660	0.1574	0.1260

5 Radiobiological Effects of Gating

Cell survival and viability were characterized using two methods common in radiation biology. Clonogenic survival is the gold standard in visualization of lack of clonogenicity following damage due to radiation. There is no distinction between cells that are clonogenically dead, and those that have undergone apoptosis. A secondary assay was used as a complement to the clonogenics – the resazurin cell viability assay (116). Resazurin, on the other hand is a measure of metabolic activity in a cell, with a presumably smaller response since cells damage by radiation can enter mitotic death – meaning they will not result in clonogens (117) – but they are still metabolically active for some time. Resazurin, a non-fluorescent salt, gets reduced into Resorufin by metabolically active cells. The proportion of active cells is obtained by measuring the fluorescence of the byproduct, Resazurin in a known concentration of cells.

5.1 Experimental Methods

H460 and HCT116 human colorectal carcinoma cells were routinely subcultured as described previously and expanded prior to all experiments. On the day of the experiment, cells were collected at a concentration of ~(0.5-1)x10^6 cells/ml in the same manner described in chapter 2. Cells were suspended and vortexed to accomplish a homogenous concentration, and 1 ml of the cell solution was placed into each experimental vial (Sarstedt 1 ml CryoPure tubes, d=12 mm, l=29 mm). Cells were kept at room temperature prior to irradiation, but placed on ice immediately following the treatment prior to plating. Each sample was irradiated with one of the gated plans for each respiratory trace.

5.1.1 Clonogenic Survival Assay

After the radiation treatment, cells were diluted and plated in triplicate in 10-cm culture dishes. The clonogenic survival assay was performed as described for FFF study in Chapter 2.

5.1.2 Resazurin Metabolic Activity Assay

Following radiation treatment, each cell sample was diluted to a concentration of 40,000 cells/ml and 500 μL of the solution was placed in one well of a 24-well plate lined with a custom glass insert. Six replicates of each sample were seeded in addition to a non-irradiated control, and the 24-well plates were

placed in a 37°C, 5% O_2, 5% CO_2 incubator for approximately 48 hours. Following this incubation, 55 µL of 2.2 mM Resazurin in phosphate-buffered saline was added to each well for a final concentration of 2.2 µM. The amount of Resofurin was measured by fluorescence using a TECAN GENios plate reader in consecutive hours following the Resazurin addition until the fluorescence of the control plateaued. The fluorescence readings were carried out with excitation λ=535 nm, emission λ=590 nm, with a 40 µs integration time and 5 flashes per well. A 3-hour (H460) and 4-hour (HCT-116) time point was chosen for the purpose of comparison between groups (see appendix for example graph of all time points).

Graphs shown represent mean ± standard deviation. Statistical analysis in the form of the unpaired t-test with Welch's correction for each gated plan vs. their nongated counterpart was performed for each respiratory trace. Asterisks on the graphs represent statistically significant differences, with all the p-values summarized in the tables that follow.

5.2 Results

A total of 6 gated samples showed statistical difference in Resazurin fluorescence from their nongated pairs in both cell lines, though there was no overlap between samples. H460 metabolism seemed to be statistically more affected by gating than in HCT116 cells. In respiratory trace 7, the fluorescence of the plan with a 30-70% gating window is most significantly different than its nongated counterpart. This respiratory trace likewise has the highest breathspeed, as summarized in Table 3.1. On average, H460 cells (Figure 5.1) showed a lower overall metabolic activity than HCT116 cells (Figure 5.2) following irradiation.

For the survival assay, H460 resulted in 10/30 of the gated treatment plans resulting in statistically different survival than the nongated plans (Figure 5.3). In HCT116 cells this was the case for 14/30 of plans (Figure 5.4). The differences in HCT116 cells were more significant than those of the H460 cells. Significance implied in figures as follows: * $p \leq 0.05$, ** $p \leq 0.01$, *** $p \leq 0.001$.

Figure 5.1 H460 Resazurin Assay Summary

H460 Resazurin fluorescence comparisons following 10 Gy of radiation delivered with nongated (-) plans and with each of the gated plans: 80-20% (1), 40-60% (2) and 30-70% (3). Asterisks represent fluorescence is significantly different than in the nongated sample of the same respiratory trace.

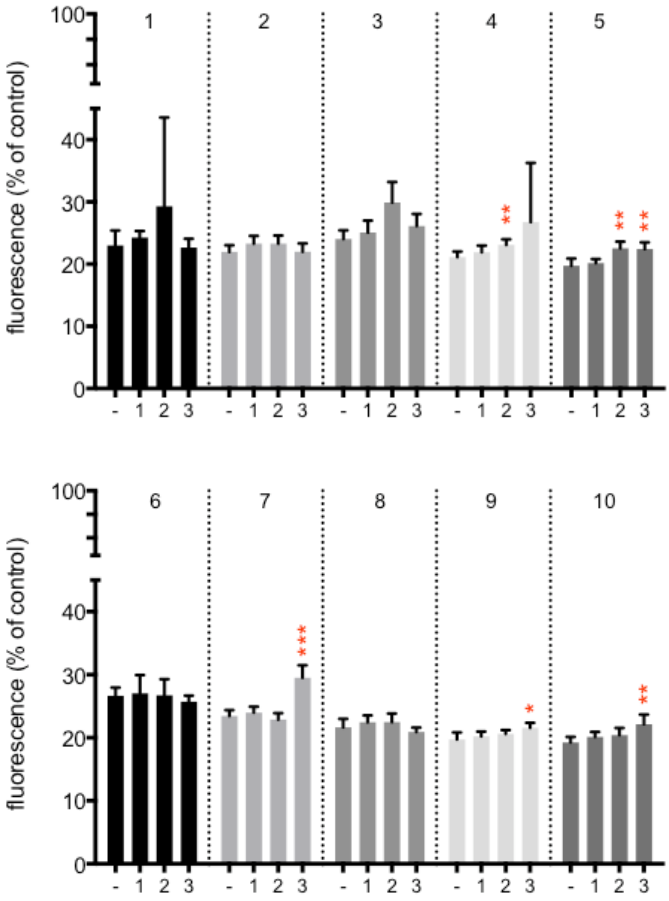

Table 5.1 H460 Resazurin assay p-values

P-values corresponding to above graphs, comparing metabolism of gated plans to nongated counterparts

Trace	1 vs -	2 vs -	3 vs -
06t	0.258	0.333	0.779
06t2	0.075	0.0835	0.978
06t3	0.317	0.0054**	0.062
16t1	0.209	0.0035**	0.209
16t2	0.439	0.0014**	0.002**
16t3	0.782	0.960	0.181
16t4	0.353	0.340	0.0002***
31t1	0.326	0.365	0.312
31t3	0.443	0.173	0.0188*
31t4	0.105	0.078	0.0037**

Figure 5.2 H4CT116 Resazurin Assay Summary

H460 Resazurin fluorescence comparisons following 10 Gy of radiation delivered with nongated (-) plans and with each of the gated plans: 80-20% (1), 40-60% (2) and 30-70% (3). Asterisks represent fluorescence is significantly different than in the nongated sample of the same respiratory trace.

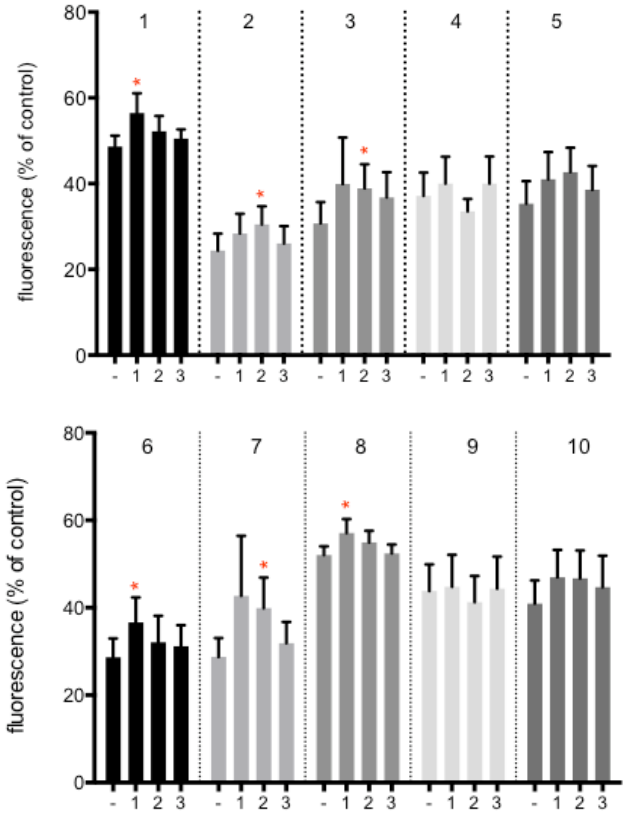

Table 5.2 HCT116 Resazurin assay p-values

P-values corresponding to above graphs, comparing metabolism of gated plans to nongated counterparts

Trace	1 vs -	2 vs -	3 vs -
06t	0.0155*	0.112	0.246
06t2	0.180	0.0456*	0.523
06t3	0.139	0.0411*	0.118
16t1	0.469	0.221	0.469
16t2	0.164	0.067	0.368
16t3	0.0395*	0.331	0.400
16t4	0.084	0.0197*	0.310
31t1	0.0197*	0.090	0.762
31t3	0.829	0.519	0.899
31t4	0.138	0.157	0.373

Figure 5.3 H460 Survival Assay Summary

H460 cell survival comparisons following 10 Gy of radiation delivered with nongated (-) plans and with each of the gated plans: 80-20% (1), 40-60% (2) and 30-70% (3). Asterisks represent survival is significantly different than in the nongated sample of the same respiratory trace.

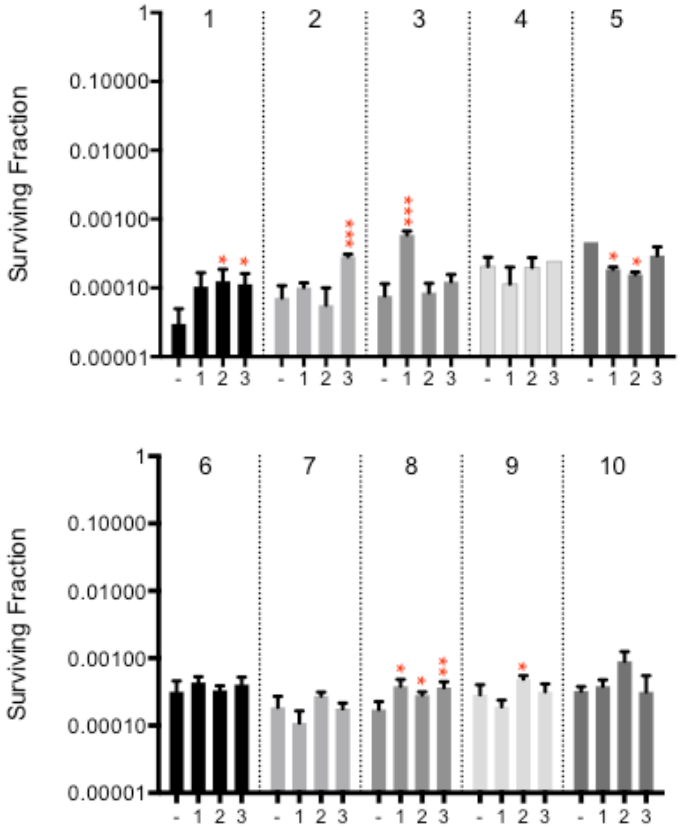

Table 5.3 H460 Clonogenic assay p-values

P-values corresponding to above graphs, comparing survival of gated plans to nongated counterparts

Trace	1 vs -	2 vs -	3 vs -
1	0.3184	0.0467*	0.0333*
2	0.2081	0.6005	0.0001***
3	0.0001***	0.7431	0.1156
4	0.3730	0.9310	0.5940
5	0.0227*	0.0192*	0.2522
6	0.4406	0.9029	0.5663
7	0.1805	0.1260	0.8718
8	0.0161*	0.0168*	0.0084**
9	0.1991	0.0303*	0.7116
10	0.5353	0.2529	0.9702

Figure 5.4 HCT116 Survival Assay Summary

HCT116 cell survival comparisons following 10 Gy of radiation delivered with nongated (-) plans and with each of the gated plans: 80-20% (1), 40-60% (2) and 30-70% (3). Asterisks represent survival is significantly different than in the nongated sample of the same respiratory trace.

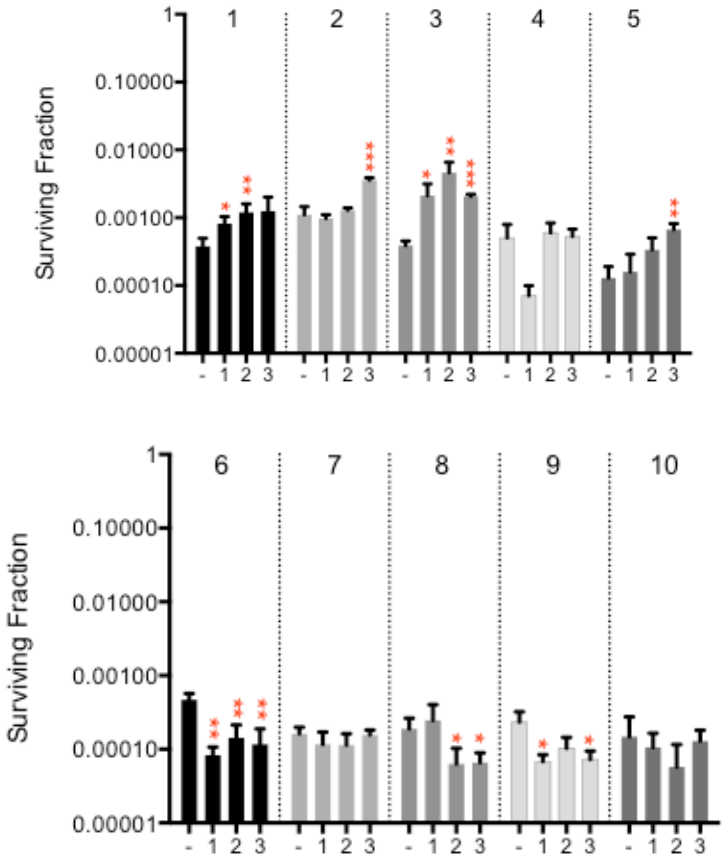

Table 5.4 HCT116 Clonogenic assay p-values

P-values corresponding to above graphs, comparing survival of gated plans to nongated counterparts

Trace	1 vs -	2 vs -	3 vs -
1	0.0190*	0.0083**	0.0614
2	0.4750	0.3142	< 0.0001***
3	0.0196*	0.0084**	< 0.0001***
4	0.0553	0.6288	0.8812
5	0.7044	0.0835	0.0026**
6	0.0027**	0.0023**	0.0016**
7	0.3020	0.2697	0.8740
8	0.5379	0.0386*	0.0412*
9	0.0314*	0.0545	0.0322*
10	0.5805	0.3013	0.8023

5.3 Discussion

As expected, the clonogenic assay showed more extreme differences in survival than the Resazurin metabolic assay. For H460 cells, both the Resazurin and clonogenic assays indicated that nongated plans resulted in the lowest cell survival/viability, while conversely gated plans with a 40-60% gating window (scheme 2) yielded highest survival. HCT116 cells exhibited a less uniform behavior dependent on the assay; Metabollic activity was lowest in nongated plans and highest in gated plans with a 80-20% gating window, while clonogenicity was lowest in the 80-20% gating window plans and highest in nongated regimes. The reversed relationship exhibited by HCT116 cells may indicate that the cells which are most damaged will be most metabolically active at time of the Resazurin assay due to various repair processes. They are however, doomed cells thus they eventually end up mitotically dead and do not form colonies. Conversely, they are less metabolically active when less repair is present thus resulting in a higher number of colonies due to less damage. It should be noted that lower amounts background staining were seen in HCT116 clonogenic plates, implying that HCT116, unlike H460 cells either undergo apoptosis or form colonies, but otherwise do not remain mitotically active and attached to plates.

More often than not Resazurin and clonogenic results for the two cell lines did not agree, which can be seen as a product of the difference in damage response in different cells. *In vitro* the proliferation rate of the lung and liver carcinoma cell lines was very similar, and visual scoring of colonies implied similar sizes in the two types of cells. For respiratory traces 4, 7 and 10, clonogenic cell survival implied no significant difference in any of the gating schemes versus the nongated plan for both H460 and HCT116 cells. No similarities in average amplitude, period, or breathing speed are found for the three traces. OSL dosimetry likewise implied that in respiratory trace 4, there were no significant differences in dose between any of the gated plans and the nongated one. Though respiratory trace 4 had large variability in the amplitude and period, its low average amplitude resulted in a low average breathing speed, a factor of dosimetric importance discussed in the following section. Viability and clonogenicity varied for the same gating window for different respiratory traces, as can be expected due to the inhomogeneity of respiration patterns.

The variation in cell survival was bigger than any of the differences observed in corresponding doses in OSL dosimetry. On a plot of cell survival versus dose, the line slope is zero to the 6^{th} decimal

place, indicating survival differences were not due to the dosimetric discrepancies observed. This suggests one of two factors is at play – OSLD readings not being representative of cell doses, or an effect different than cumulative dose being responsible for the difference in survival. The first may occur due to cell aggregation. The surface area of an OSL nanodot is 44 mm^2, however if ~1 million cells aggregates completely, they can form spheroids 1 mm in diameter. If such a cell cluster was being under, or conversely overdosed it would be difficult to measure the precise dose with the larger OSLD. The contour for the GTV was done in accordance to the CT outline of the cell vial, which has a much larger volume (~3.27 cm^3) than the OSLD (~5.9 mm^3). It is thus more likely that the OSLD will remain within the margins of the PTV even though it moves, unlike the larger cell vial. The margin extended from the GTV in all ten cases may not have been enough to account for the sup-inf motion of the vial, which is in excess of 6 mm.

The interplay effect has been discussed in numerous recent publications (118-120), addressing the issue with the directionality of MLC motion in relation to the motion of a tumour. The resultant dose coverage is dependent on the symmetry of the tumour as well as the extent of its motion and that of the MLC. The MLC leaves moving in the same direction as the tumour, as seen in Figure 5.5 (b) can contribute to a greater discrepancy in dose coverage than if they are moving perpendicularly to the tumour (Figure 5.5 (a)). Axes of symmetry in the shape of a PTV can also play a role in the interplay effect, a moving tumour that tapers at one end may get a significantly lower dose than prescribed, or conversely a larger volume of normal tissue may receive a larger dose than allowed. Though the approximately cylindrical PTV contoured in these experiments had symmetry along the x,y, and z axes, it was not uniform in the plane of he collimator, at 35° , as is shown in Figure 5.5 (c).

Figure 5.5 The interplay effect
Multileaf collimator motion shown in conjunction with GTV motion

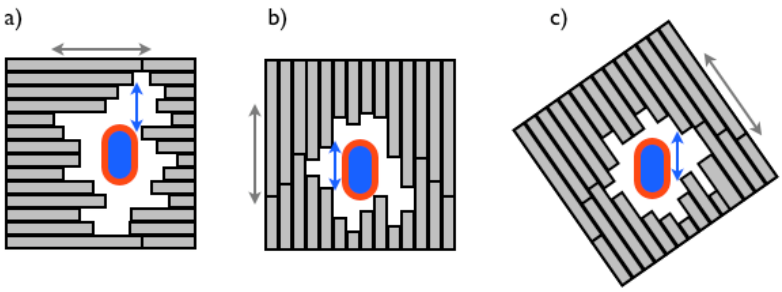

Bortfeld *et al.* (100) found that the delivery error peaks when the scanning period of the MLCs is approximately the same duration as the breathing motion speed. A difficulty arises in calculating the exact scanning period of the MLCs in non-trivial plans having shapes more complicated than a rectangle, and particularly for gated plans where scanning of the MLC is repeatedly interrupted for beam-holds. If we make the assumption that the scanning speed is approximately the same for all the nongated plans of the ten respiratory traces, we can compare how dose and survival fare with the breathing speed, as summarized in Table 3.1. We can assume that the scanning speed is uniform, and at least an order of magnitude slower than any single breathing speed. In such a case, the smaller the breathing speed, the larger the discrepancy in dose delivered. Figure 5.6 shows a plot of the percent dose discrepancy (defined as : $(D_{ECLIPSE} - D_{OSLD})/D_{ECLIPSE}$) versus the breathing speed as described earlier. The relationship supports the theory of Bortfeld *et al*. showing a mildly negative relationship, albeit with a poor R^2 of 0.1.

Figure 5.6 OSL dose versus breathing speed graph
A linear relationship is seen, with dose discrepancy decreasing as breathing speed increases.

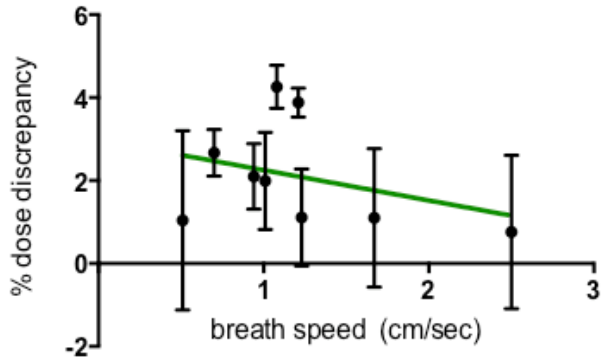

Clonogenic cell survival in HCT116 and H460 cells likewise shows a gradual decline with breathing speed, as seen in Figure 5.7, much like the OSLD dose, in agreement with the dose discrepancy and the interplay theory.

Figure 5.7 Cell survival versus breathing speed graph

Decreasing cell survival is seen in (a) H460 and (b) HCT116 cells as breathing speed increases.

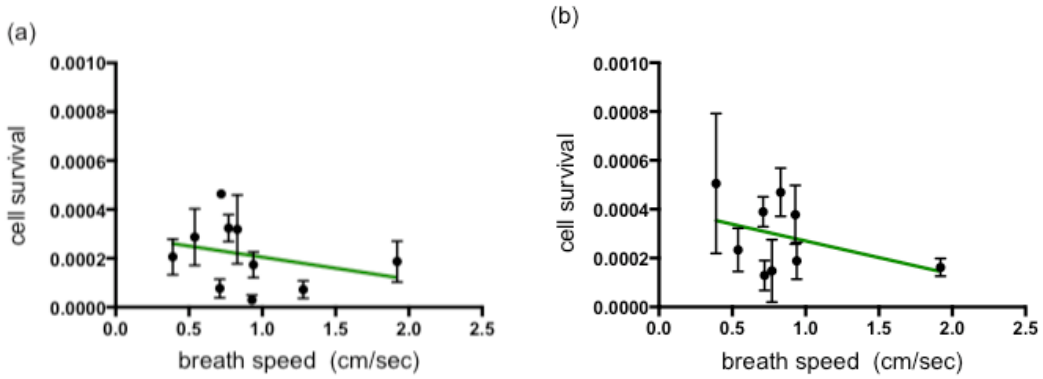

The other factor that may have modified dose response more so than would be indicative of the dose discrepancies may have been the radiobiological effects occurring due to dose protraction. The agreement in cell viability and the colony assay was not observed for a majority of instances, indicating that metabolic activity in this case was not a good predictor of clonogenic cell survival for both H460 and HCT116 cells. In both cell lines some amount of 'background staining' was noticed, where cells that did not form colonies or undergo apoptosis simply remained attached to plates but were otherwise mitotically dead. Such cells would be deemed viable via the Resazurin assay, however they are assumed as 'dead' by the clonogenic assay.

6 Conclusions and further work

6.1 Conclusions

The use of FFF photon mode to effectively decrease treatment time, in particular for gating applications has been substantiated in this work. The feasibility of applying gated treatments in FFF mode on the TrueBeam linear accelerator has been validated for 10 MV photons. Most dose discrepancies, save for one case, remained under 5% of the prescribed dose, which is an acceptable uncertainty in SBRT treatments. The differences between the planned and OSLD doses were largely below 30 cGy, a dose not associated with differences in radiobiological response.

There is a large variety of dosimetric as well as radiobiological effects affecting gated regimens of radiation therapy such that distinguishing them is a difficult task. It is evident that in certain cases gating allows for a more effective dose response, reproducing the predicted conditions more closely than the nongated plans. No single factor, including respiration amplitude and phase, breathing speed, motion extent or the level of consistency was able to describe which cases would benefit from gating, and less so which gating window provided the best results. This does not completely discount that an effect exists; it may solely be too small to be seen in a sample size of 10 respiratory traces. More effort needs to be placed on quantifying the interplay effect in dynamic MLC treatments, as it emerged here as a predictor of dose to the PTV given a certain breathing speed.

The effects seen in cell survival and viability for H460 and HCT116 human carcinomas were too large to be attributed to dosimetric differences, although it is acknowledged the dosimeters did not account for inhomogeneity in tumour dose coverage. The finite size of OSLDs in the study proved a challenge, but their use was substantiated by relatively homogenous PTV coverage. Inconsistencies in the results of the metabolic and clonogenic assays for both cell lines emphasized the differences in radiation damage response. Both cell lines had differences in nongated vs. gated plans of the same respiratory trace that reached statistical significance. This may have further implications in the radiobiological response to gating, although a need to verify with various cell lines and an *in vivo* model arises.

6.2 Future work

All the work in the above thesis was done with respiratory traces of non-trained patients. It has recently been documented that a vast improvement in the regularity of respiration has been shown for recordings utilizing training in way of audio instructions or visual feedback, for example (121-123). In this way, some consistency is retained throughout treatment, if breathing during 4DCT image acquisition is similar to that during treatment. Training would reduce inconsistency in CT imaging, lessening the number of reconstruction artefacts, which improves treatment planning and delivery. Training likewise improves accuracy in breath-hold techniques, which is another 4D treatment method that may reduce treatment time and improve accuracy. In breath-hold techniques where respiration amplitude is tracked, the precise assignment of beam-on and off amplitudes is crucial as the windows generally last more than the gating windows in this study, which were less than 2 seconds. A rapid and effective evaluation of how well a patient may adhere to the respiratory training/guidance prior to beginning the 4D imaging and treatment is in such cases required.

Fiducial-based systems are emerging as the preferred method of gating, with continuous in-treatment imaging and image-matching to ensure the fiducial is in the same location as when the dose was prescribed. The additional imaging dose and implantation procedure of such a treatment can be avoided by further exploration of non-invasive surrogate tracking in order to improve it.

The major consideration that was not discussed in this work is dose to normal tissues surrounding a tumour. The predominantly favorable outcomes in PTV coverage presented in the above study warrant the precise evaluation of doses surrounding the target. For such a study, planning with more stringent constraints on surrounding volumes and likely an increased field complexity would be required. Furthermore, a point dose measurement as employed here would no longer be acceptable. Multi-dimensional dosimeters such as Gafchromic film or polymer gels may be used to account for volume effects, which are of importance in the liver.

References

1. Blomgren H, Lax I, Naslund I, *et al.* Stereotactic high dose fraction radiation therapy of extracranial tumors using an accelerator. Clinical experience of the first thirty-one patients. *Acta Oncol* 1995;34:861-870.
2. Chang BK, Timmerman RD. Stereotactic body radiation therapy: a comprehensive review. *Am J Clin Oncol* 2007;30:637-644.
3. Hayman JA, Martel MK, Ten Haken RK, *et al.* Dose escalation in non-small-cell lung cancer using three-dimensional conformal radiation therapy: update of a phase I trial. *J Clin Oncol* 2001;19:127-136.
4. Rosenzweig KE, Fox JL, Yorke E, *et al.* Results of a phase I dose-escalation study using three-dimensional conformal radiotherapy in the treatment of inoperable nonsmall cell lung carcinoma. *Cancer* 2005;103:2118-2127.
5. Timmerman R, Papiez L, McGarry R, *et al.* Extracranial stereotactic radioablation: results of a phase I study in medically inoperable stage I non-small cell lung cancer. *Chest* 2003;124:1946-1955.
6. Timmerman R, McGarry R, Yiannoutsos C, *et al.* Excessive toxicity when treating central tumors in a phase II study of stereotactic body radiation therapy for medically inoperable early-stage lung cancer. *J Clin Oncol* 2006;24:4833-4839.
7. Louie AV, Rodrigues G, Hannouf M, *et al.* Stereotactic body radiotherapy versus surgery for medically operable Stage I non-small-cell lung cancer: a Markov model-based decision analysis. *Int J Radiat Oncol Biol Phys* 2011;81:964-973.
8. Onishi H, Shirato H, Nagata Y, *et al.* Stereotactic body radiotherapy (SBRT) for operable stage I non-small-cell lung cancer: can SBRT be comparable to surgery? *Int J Radiat Oncol Biol Phys* 2011;81:1352-1358.
9. Lagerwaard FJ, Haasbeek CJ, Smit EF, *et al.* Outcomes of risk-adapted fractionated stereotactic radiotherapy for stage I non-small-cell lung cancer. *Int J Radiat Oncol Biol Phys* 2008;70:685-692.

10. Fakiris AJ, McGarry RC, Yiannoutsos CT, *et al.* Stereotactic body radiation therapy for early-stage non-small-cell lung carcinoma: four-year results of a prospective phase II study. *Int J Radiat Oncol Biol Phys* 2009;75:677-682.

11. Baumann P, Nyman J, Hoyer M, *et al.* Outcome in a prospective phase II trial of medically inoperable stage I non-small-cell lung cancer patients treated with stereotactic body radiotherapy. *J Clin Oncol* 2009;27:3290-3296.

12. Timmerman R, Paulus R, Galvin J, *et al.* Stereotactic body radiation therapy for inoperable early stage lung cancer. *JAMA* 2010;303:1070-1076.

13. Benedict SH, Yenice KM, Followill D, *et al.* Stereotactic body radiation therapy: the report of AAPM Task Group 101. *Med Phys* 2010;37:4078-4101.

14. Park HJ, Griffin RJ, Hui S, *et al.* Radiation-induced vascular damage in tumors: implications of vascular damage in ablative hypofractionated radiotherapy (SBRT and SRS). *Radiat Res* 2012;177:311-327.

15. Garcia-Barros M, Paris F, Cordon-Cardo C, *et al.* Tumor response to radiotherapy regulated by endothelial cell apoptosis. *Science* 2003;300:1155-1159.

16. Formenti SC, Demaria S. Systemic effects of local radiotherapy. *Lancet Oncol* 2009;10:718-726.

17. Amundson SA, Grace MB, McLeland CB, *et al.* Human in vivo radiation-induced biomarkers: gene expression changes in radiotherapy patients. *Cancer Res* 2004;64:6368-6371.

18. Goodman KA, Wiegner EA, Maturen KE, *et al.* Dose-escalation study of single-fraction stereotactic body radiotherapy for liver malignancies. *Int J Radiat Oncol Biol Phys*;78:486-493.

19. elSaadany S, Tepper M, Mao Y, *et al.* An epidemiologic study of hepatocellular carcinoma in Canada. *Can J Public Health* 2002;93:443-446.

20. Taylor I. Liver metastases from colorectal cancer: lessons from past and present clinical studies. *Br J Surg* 1996;83:456-460.

21. Silverthorn DU. Human physiology : an integrated approach. 4th ed. San Francisco: Pearson/Benjamin Cummings; 2007.

22. Tse RV, Hawkins M, Lockwood G*, et al.* Phase I study of individualized stereotactic body radiotherapy for hepatocellular carcinoma and intrahepatic cholangiocarcinoma. *J Clin Oncol* 2008;26:657-664.

23. Lee MT, Kim JJ, Dinniwell R*, et al.* Phase I study of individualized stereotactic body radiotherapy of liver metastases. *J Clin Oncol* 2009;27:1585-1591.

24. Blumgart LH, Fong Y, Jarnagin WR*, et al.* Hepatobiliary cancer. Hamilton, Ont.Lewiston, NY: B C Decker :Sales and distribution, US, B.C. Decker; 2001.

25. Kopek N, Holt MI, Hansen AT*, et al.* Stereotactic body radiotherapy for unresectable cholangiocarcinoma. *Radiother Oncol*;94:47-52.

26. Mancosu P, Castiglioni S, Reggiori G*, et al.* Stereotactic body radiation therapy for liver tumours using flattening filter free beam: dosimetric and technical considerations. *Radiat Oncol* 2012;7:16.

27. Levitt SH. Technical basis of radiation therapy : practical clinical applications. 4th rev. ed. Berlin ; New York: Springer; 2006.

28. Hawkins MA, Dawson LA. Radiation therapy for hepatocellular carcinoma: from palliation to cure. *Cancer* 2006;106:1653-1663.

29. Yamasaki SA, Marn CS, Francis IR*, et al.* High-dose localized radiation therapy for treatment of hepatic malignant tumors: CT findings and their relation to radiation hepatitis. *AJR Am J Roentgenol* 1995;165:79-84.

30. Lawrence TS, Robertson JM, Anscher MS*, et al.* Hepatic toxicity resulting from cancer treatment. *Int J Radiat Oncol Biol Phys* 1995;31:1237-1248.

31. Guha C, Kavanagh BD. Hepatic radiation toxicity: avoidance and amelioration. *Semin Radiat Oncol* 2011;21:256-263.

32. Dawson LA, Normolle D, Balter JM*, et al.* Analysis of radiation-induced liver disease using the Lyman NTCP model. *Int J Radiat Oncol Biol Phys* 2002;53:810-821.

33. Pan CC, Kavanagh BD, Dawson LA*, et al.* Radiation-associated liver injury. *Int J Radiat Oncol Biol Phys* 2010;76:S94-100.

34. Schefter TE, Kavanagh BD. Radiation therapy for liver metastases. *Semin Radiat Oncol* 2011;21:264-270.

35. Rule W, Timmerman R, Tong L, *et al.* Phase I dose-escalation study of stereotactic body radiotherapy in patients with hepatic metastases. *Ann Surg Oncol* 2011;18:1081-1087.

36. Rusthoven KE, Kavanagh BD, Burri SH, *et al.* Multi-institutional phase I/II trial of stereotactic body radiation therapy for lung metastases. *J Clin Oncol* 2009;27:1579-1584.

37. Schefter TE, Kavanagh BD, Timmerman RD, *et al.* A phase I trial of stereotactic body radiation therapy (SBRT) for liver metastases. *Int J Radiat Oncol Biol Phys* 2005;62:1371-1378.

38. Herfarth KK, Hof H, Bahner ML, *et al.* Assessment of focal liver reaction by multiphasic CT after stereotactic single-dose radiotherapy of liver tumors. *Int J Radiat Oncol Biol Phys* 2003;57:444-451.

39. Johnson PJ, Williams R. Serum alpha-fetoprotein estimations and doubling time in hepatocellular carcinoma: influence of therapy and possible value in early detection. *J Natl Cancer Inst* 1980;64:1329-1332.

40. Trott KR, Kummermehr J. Rapid repopulation in radiotherapy: a debate on mechanism. Accelerated repopulation in tumours and normal tissues. *Radiother Oncol* 1991;22:159-160.

41. Russell AH, Clyde C, Wasserman TH, *et al.* Accelerated hyperfractionated hepatic irradiation in the management of patients with liver metastases: results of the RTOG dose escalating protocol. *Int J Radiat Oncol Biol Phys* 1993;27:117-123.

42. Taylor JM, Withers HR, Mendenhall WM. Dose-time considerations of head and neck squamous cell carcinomas treated with irradiation. *Radiother Oncol* 1990;17:95-102.

43. Saunders M, Dische S, Barrett A, *et al.* Continuous, hyperfractionated, accelerated radiotherapy (CHART) versus conventional radiotherapy in non-small cell lung cancer: mature data from the randomised multicentre trial. CHART Steering committee. *Radiother Oncol* 1999;52:137-148.

44. Mehta M, Scrimger R, Mackie R, *et al.* A new approach to dose escalation in non-small-cell lung cancer. *Int J Radiat Oncol Biol Phys* 2001;49:23-33.

45. Dische S, Saunders M, Barrett A, *et al.* A randomised multicentre trial of CHART versus conventional radiotherapy in head and neck cancer. *Radiother Oncol* 1997;44:123-136.

46. Williams MV, Denekamp J, Fowler JF. A review of alpha/beta ratios for experimental tumors: implications for clinical studies of altered fractionation. *Int J Radiat Oncol Biol Phys* 1985;11:87-96.

47. Ruggieri R, Stavreva N, Naccarato S*, et al.* Computed 88% TCP dose for SBRT of NSCLC from tumour hypoxia modelling. *Phys Med Biol* 2013;58:4611-4620.

48. Cheng JC, Wu JK, Huang CM*, et al.* Dosimetric analysis and comparison of three-dimensional conformal radiotherapy and intensity-modulated radiation therapy for patients with hepatocellular carcinoma and radiation-induced liver disease. *Int J Radiat Oncol Biol Phys* 2003;56:229-234.

49. Wu VW, Kwong DL, Sham JS. Target dose conformity in 3-dimensional conformal radiotherapy and intensity modulated radiotherapy. *Radiother Oncol* 2004;71:201-206.

50. Verbakel WF, Senan S, Cuijpers JP*, et al.* Rapid delivery of stereotactic radiotherapy for peripheral lung tumors using volumetric intensity-modulated arcs. *Radiother Oncol* 2009;93:122-124.

51. Dunlap NE, Cai J, Biedermann GB*, et al.* Chest wall volume receiving >30 Gy predicts risk of severe pain and/or rib fracture after lung stereotactic body radiotherapy. *Int J Radiat Oncol Biol Phys*;76:796-801.

52. Pettersson N, Nyman J, Johansson KA. Radiation-induced rib fractures after hypofractionated stereotactic body radiation therapy of non-small cell lung cancer: a dose- and volume-response analysis. *Radiother Oncol* 2009;91:360-368.

53. Voroney JP, Hope A, Dahele MR*, et al.* Chest wall pain and rib fracture after stereotactic radiotherapy for peripheral non-small cell lung cancer. *J Thorac Oncol* 2009;4:1035-1037.

54. Keall PJ, Mageras GS, Balter JM*, et al.* The management of respiratory motion in radiation oncology report of AAPM Task Group 76. *Med Phys* 2006;33:3874-3900.

55. Biancia CD, Yorke E, Chui CS*, et al.* Comparison of end normal inspiration and expiration for gated intensity modulated radiation therapy (IMRT) of lung cancer. *Radiother Oncol* 2005;75:149-156.

56. Wolthaus JW, Sonke JJ, van Herk M*, et al.* Comparison of different strategies to use four-dimensional computed tomography in treatment planning for lung cancer patients. *Int J Radiat Oncol Biol Phys* 2008;70:1229-1238.

57. Naylor CD. The rational clinical examination. Physical examination of the liver. *JAMA* 1994;271:1859-1865.

58. Langen KM, Jones DT. Organ motion and its management. *Int J Radiat Oncol Biol Phys* 2001;50:265-278.

59. Scorsetti M, Alongi F, Castiglioni S*, et al.* Feasibility and early clinical assessment of flattening filter free (FFF) based stereotactic body radiotherapy (SBRT) treatments. *Radiat Oncol* 2011;6:113.

60. Reggiori G, Mancosu P, Castiglioni S*, et al.* Can volumetric modulated arc therapy with flattening filter free beams play a role in stereotactic body radiotherapy for liver lesions? A volume-based analysis. *Med Phys*;39:1112-1118.

61. Georg D, Kragl G, Wetterstedt S*, et al.* Photon beam quality variations of a flattening filter free linear accelerator. *Med Phys* 2010;37:49-53.

62. Georg D, Kragl G, Wetterstedt S*, et al.* Photon beam quality variations of a flattening filter free linear accelerator. *Med Phys* 2010;37:49-53.

63. Kragl G, af Wetterstedt S, Knausl B*, et al.* Dosimetric characteristics of 6 and 10MV unflattened photon beams. *Radiother Oncol* 2009;93:141-146.

64. Cashmore J. The characterization of unflattened photon beams from a 6 MV linear accelerator. *Phys Med Biol* 2008;53:1933-1946.

65. Khan FM, Gibbons JP, Roback DM. Collimator (head) scatter at extended distances in linear accelerator-generated photon beams. *Int J Radiat Oncol Biol Phys* 1996;35:605-608.

66. Palma DA, Verbakel WF, Otto K*, et al.* New developments in arc radiation therapy: a review. *Cancer Treat Rev* 2010;36:393-399.

67. Murthy V, Gupta T, Kadam A*, et al.* Time trial: a prospective comparative study of the time-resource burden for three-dimensional conformal radiotherapy and intensity-modulated radiotherapy in head and neck cancers. *J Cancer Res Ther* 2009;5:107-112.

68. Miles EA, Clark CH, Urbano MT, *et al.* The impact of introducing intensity modulated radiotherapy into routine clinical practice. *Radiother Oncol* 2005;77:241-246.

69. Palma D, Vollans E, James K, *et al.* Volumetric modulated arc therapy for delivery of prostate radiotherapy: comparison with intensity-modulated radiotherapy and three-dimensional conformal radiotherapy. *Int J Radiat Oncol Biol Phys* 2008;72:996-1001.

70. Cozzi L, Dinshaw KA, Shrivastava SK, *et al.* A treatment planning study comparing volumetric arc modulation with RapidArc and fixed field IMRT for cervix uteri radiotherapy. *Radiother Oncol* 2008;89:180-191.

71. Elmore E, Lao XY, Kapadia R, *et al.* The effect of dose rate on radiation-induced neoplastic transformation in vitro by low doses of low-LET radiation. *Radiat Res* 2006;166:832-838.

72. Hall EJ. Radiation dose-rate: a factor of importance in radiobiology and radiotherapy. *Br J Radiol* 1972;45:81-97.

73. Hall EJ, Brenner DJ. The dose-rate effect revisited: radiobiological considerations of importance in radiotherapy. *Int J Radiat Oncol Biol Phys* 1991;21:1403-1414.

74. Steel GG, Deacon JM, Duchesne GM, *et al.* The dose-rate effect in human tumour cells. *Radiother Oncol* 1987;9:299-310.

75. Steel GG, Down JD, Peacock JH, *et al.* Dose-rate effects and the repair of radiation damage. *Radiother Oncol* 1986;5:321-331.

76. van den Aardweg GJ, Hopewell JW. The kinetics of repair for sublethal radiation-induced damage in the pig epidermis: an interpretation based on a fast and a slow component of repair. *Radiother Oncol* 1992;23:94-104.

77. Ang KK, Jiang GL, Guttenberger R, *et al.* Impact of spinal cord repair kinetics on the practice of altered fractionation schedules. *Radiother Oncol* 1992;25:287-294.

78. Turesson I, Thames HD. Repair capacity and kinetics of human skin during fractionated radiotherapy: erythema, desquamation, and telangiectasia after 3 and 5 year's follow-up. *Radiother Oncol* 1989;15:169-188.

79. van Rongen E, Thames HD, Jr., Travis EL. Recovery from radiation damage in mouse lung: interpretation in terms of two rates of repair. *Radiat Res* 1993;133:225-233.

80. Thames HD, Bentzen SM, Turesson I*, et al.* Fractionation parameters for human tissues and tumors. *Int J Radiat Biol* 1989;56:701-710.

81. Ling CC, Gerweck LE, Zaider M*, et al.* Dose-rate effects in external beam radiotherapy redux. *Radiother Oncol* 2010;95:261-268.

82. Furre T, Koritzinsky M, Olsen DR*, et al.* Inverse dose-rate effect due to pre-mitotic accumulation during continuous low dose-rate irradiation of cervix carcinoma cells. *Int J Radiat Biol* 1999;75:699-707.

83. Hypoxia-mediated chronic normal tissue injury. *J Support Oncol* 2004;2:433-434, 437.

84. Ling CC, Spiro IJ, Stickler R. Dose-rate effect between 1 and 10 Gy/min in mammalian cell culture. *Br J Radiol* 1984;57:723-728.

85. Hall EJ. Radiobiology for the radiologist. 4th ed. Philadelphia: J.B. Lippincott; 1994.

86. Johns HE, Cunningham JR. The physics of radiology. 4th ed. Springfield, Ill., U.S.A.: Charles C. Thomas; 1983.

87. Nias AHW. An introduction to radiobiology. Chichester ; New York: Wiley; 1990.

88. Roots R, Okada S. Estimation of life times and diffusion distances of radicals involved in x-ray-induced DNA strand breaks of killing of mammalian cells. *Radiat Res* 1975;64:306-320.

89. Markova E, Torudd J, Belyaev I. Long time persistence of residual 53BP1/gamma-H2AX foci in human lymphocytes in relationship to apoptosis, chromatin condensation and biological dosimetry. *Int J Radiat Biol* 2011;87:736-745.

90. Kotte AN, Hofman P, Lagendijk JJ*, et al.* Intrafraction motion of the prostate during external-beam radiation therapy: analysis of 427 patients with implanted fiducial markers. *Int J Radiat Oncol Biol Phys* 2007;69:419-425.

91. Shirato H, Suzuki K, Sharp GC*, et al.* Speed and amplitude of lung tumor motion precisely detected in four-dimensional setup and in real-time tumor-tracking radiotherapy. *Int J Radiat Oncol Biol Phys* 2006;64:1229-1236.

92. Delouya G, Carrier JF, Beliveau-Nadeau D*, et al.* Migration of intraprostatic fiducial markers and its influence on the matching quality in external beam radiation therapy for prostate cancer. *Radiother Oncol*;96:43-47.

93. Kitamura K, Shirato H, Shimizu S*, et al.* Registration accuracy and possible migration of internal fiducial gold marker implanted in prostate and liver treated with real-time tumor-tracking radiation therapy (RTRT). *Radiother Oncol* 2002;62:275-281.

94. Shchory T, Schifter D, Lichtman R*, et al.* Tracking accuracy of a real-time fiducial tracking system for patient positioning and monitoring in radiation therapy. *Int J Radiat Oncol Biol Phys*;78:1227-1234.

95. Willoughby TR, Forbes AR, Buchholz D*, et al.* Evaluation of an infrared camera and X-ray system using implanted fiducials in patients with lung tumors for gated radiation therapy. *Int J Radiat Oncol Biol Phys* 2006;66:568-575.

96. Meeks SL, Bova FJ, Wagner TH*, et al.* Image localization for frameless stereotactic radiotherapy. *Int J Radiat Oncol Biol Phys* 2000;46:1291-1299.

97. Yu C, Main W, Taylor D*, et al.* An anthropomorphic phantom study of the accuracy of Cyberknife spinal radiosurgery. *Neurosurgery* 2004;55:1138-1149.

98. Murphy MJ, Cox RS. The accuracy of dose localization for an image-guided frameless radiosurgery system. *Med Phys* 1996;23:2043-2049.

99. Watanabe Y. Derivation of linear attenuation coefficients from CT numbers for low-energy photons. *Phys Med Biol* 1999;44:2201-2211.

100. Bortfeld T, Jiang SB, Rietzel E. Effects of motion on the total dose distribution. *Semin Radiat Oncol* 2004;14:41-51.

101. Mageras GS, Yorke E. Deep inspiration breath hold and respiratory gating strategies for reducing organ motion in radiation treatment. *Semin Radiat Oncol* 2004;14:65-75.

102. Hrbacek J, Lang S, Klock S. Commissioning of photon beams of a flattening filter-free linear accelerator and the accuracy of beam modeling using an anisotropic analytical algorithm. *Int J Radiat Oncol Biol Phys*;80:1228-1237.

103. Nicolini G, Vanetti E, Clivio A*, et al.* The GLAaS algorithm for portal dosimetry and quality assurance of RapidArc, an intensity modulated rotational therapy. *Radiat Oncol* 2008;3:24.

104. Otto K. Letter to the Editor on 'Single-Arc IMRT?'. *Phys Med Biol* 2009;54:L37-41; author reply L43-34.

105. Balagamwala EH, Suh JH, Barnett GH*, et al.* The importance of the conformality, heterogeneity, and gradient indices in evaluating Gamma Knife radiosurgery treatment plans for intracranial meningiomas. *Int J Radiat Oncol Biol Phys*;83:1406-1413.

106. Taylor ML, Kron T, Franich RD. A contemporary review of stereotactic radiotherapy: inherent dosimetric complexities and the potential for detriment. *Acta Oncol*;50:483-508.

107. Das IJ, Ding GX, Ahnesjo A. Small fields: nonequilibrium radiation dosimetry. *Med Phys* 2008;35:206-215.

108. Heydarian M, Hoban PW, Beddoe AH. A comparison of dosimetry techniques in stereotactic radiosurgery. *Phys Med Biol* 1996;41:93-110.

109. Reft CS. The energy dependence and dose response of a commercial optically stimulated luminescent detector for kilovoltage photon, megavoltage photon, and electron, proton, and carbon beams. *Med Phys* 2009;36:1690-1699.

110. Allen PD, Chaudhri MA. Production of neutrons from water, polyethylene, tissue equivalent material and CR-39 irradiated with 2.5-30 MeV photons. *Australas Phys Eng Sci Med* 1991;14:153-156.

111. Yukihara EG, Gasparian PBR, Sawakuchi GO*, et al.* Medical applications of optically stimulated luminescence dosimeters (OSLDs). *Radiation Measurements* 2010;45:658-662.

112. Aznar MC, Andersen CE, Botter-Jensen L*, et al.* Real-time optical-fibre luminescence dosimetry for radiotherapy: physical characteristics and applications in photon beams. *Phys Med Biol* 2004;49:1655-1669.

113. Viamonte A, da Rosa LA, Buckley LA*, et al.* Radiotherapy dosimetry using a commercial OSL system. *Med Phys* 2008;35:1261-1266.

114. Jursinic PA. Changes in optically stimulated luminescent dosimeter (OSLD) dosimetric characteristics with accumulated dose. *Med Phys*;37:132-140.

115. Wink N, Panknin C, Solberg TD. Phase versus amplitude sorting of 4D-CT data. *J Appl Clin Med Phys* 2006;7:77-85.

116. Anoopkumar-Dukie S, Carey JB, Conere T*, et al.* Resazurin assay of radiation response in cultured cells. *Br J Radiol* 2005;78:945-947.

117. Ross GM. Induction of cell death by radiotherapy. *Endocr Relat Cancer* 1999;6:41-44.

118. Berbeco RI, Pope CJ, Jiang SB. Measurement of the interplay effect in lung IMRT treatment using EDR2 films. *J Appl Clin Med Phys* 2006;7:33-42.

119. Chen H, Wu A, Brandner ED*, et al.* Dosimetric evaluations of the interplay effect in respiratory-gated intensity-modulated radiation therapy. *Med Phys* 2009;36:893-903.

120. Ong C, Verbakel WF, Cuijpers JP*, et al.* Dosimetric impact of interplay effect on RapidArc lung stereotactic treatment delivery. *Int J Radiat Oncol Biol Phys*;79:305-311.

121. Neicu T, Berbeco R, Wolfgang J*, et al.* Synchronized moving aperture radiation therapy (SMART): improvement of breathing pattern reproducibility using respiratory coaching. *Phys Med Biol* 2006;51:617-636.

122. Kini VR, Vedam SS, Keall PJ*, et al.* Patient training in respiratory-gated radiotherapy. *Med Dosim* 2003;28:7-11.

123. Vedam SS, Kini VR, Keall PJ*, et al.* Quantifying the predictability of diaphragm motion during respiration with a noninvasive external marker. *Med Phys* 2003;30:505-513.

Appendix

A. Additional data

Figure A.1: Example Dose Volume Histogram for trace 1 – plan with an 80-20% gating window

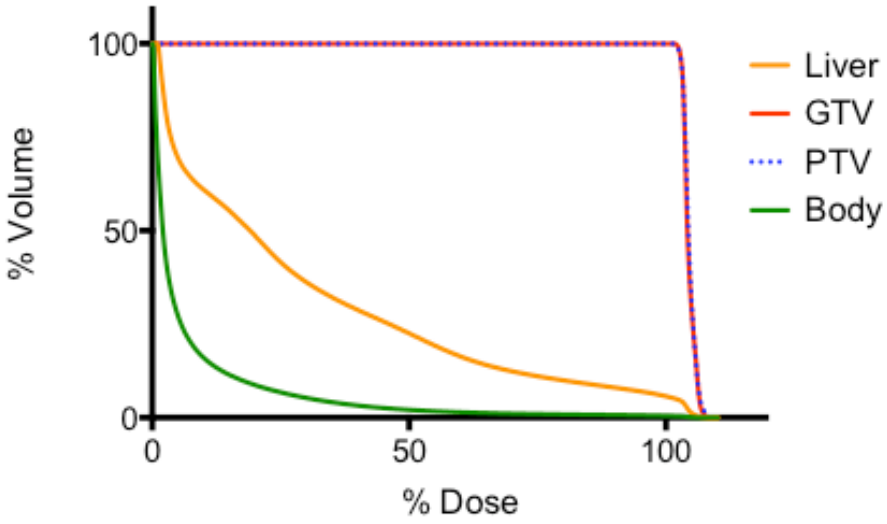

Figure A.2: Resorufin fluorescence timecourse graphs